ORIGINAL RESEARCH ARTICLE

Failure Study of Creep and High-Temperature Tensile Tested Tungsten Inert Gas Welded P92 Steel and AISI 304L Steel Dissimilar Weld Joints
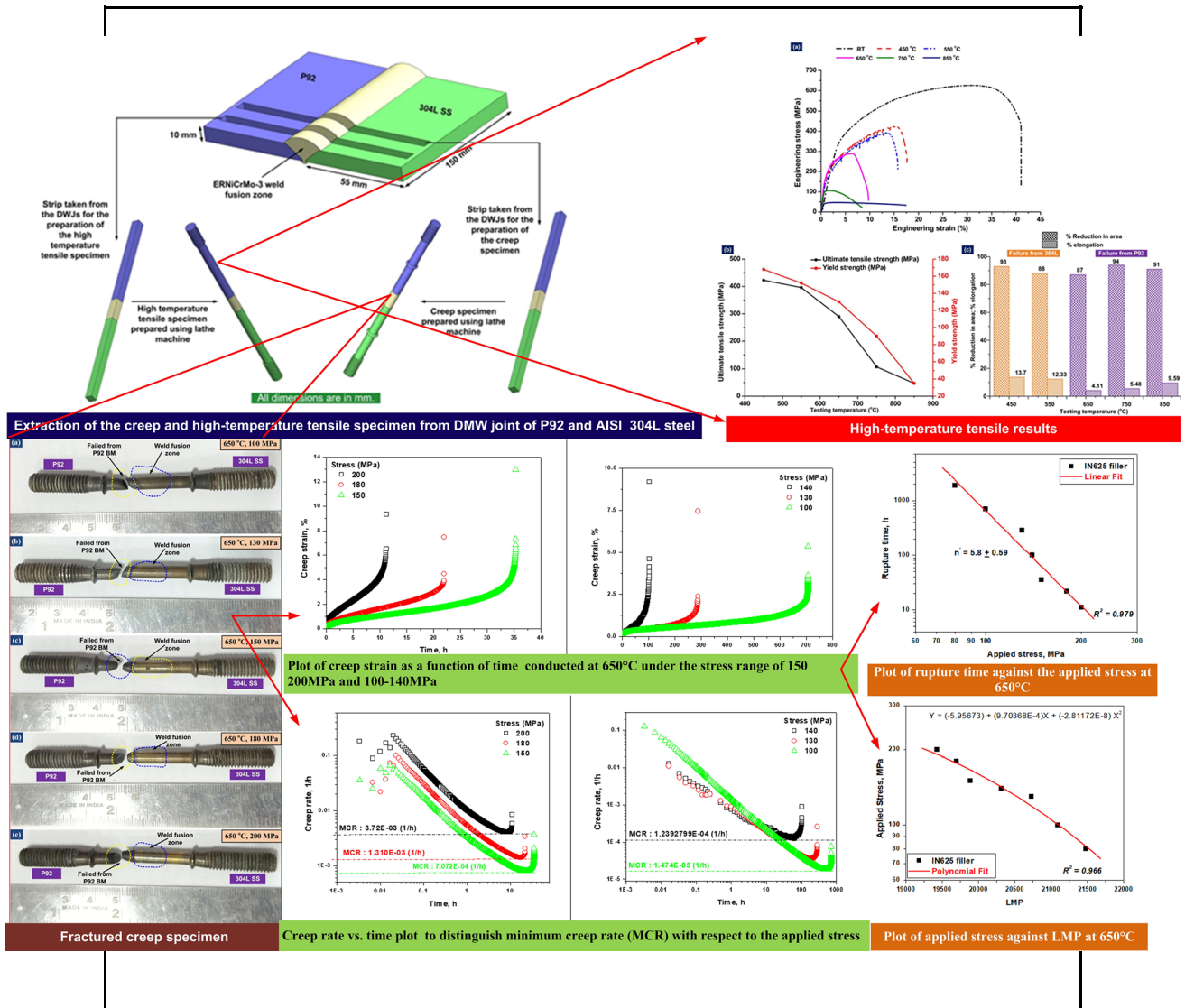
Gaurav Dak, Krishna Guguloth, Abir Bhattacharyya, Pradeep Kumar, and Chandan Pandey

The present study explores the creep and high-temperature tensile performance of the P92/304L dissimilar weld joint. The gas tungsten arc welding (GTAW) technique was used to prepare the dissimilar weld joint between P92 creep strength enhanced ferritic (CSEF) steel and 304L austenitic stainless steel (SS) by utilizing ERNiCrMo-3 filler metal. After welding, tensile strength was evaluated at 450, 550, 650, 750, and 850 °C temperature to examine the performance of the dissimilar weld joint at elevated temperatures. The high-temperature tensile test result indicated that the ultimate tensile strength (UTS) decreased from 439 to 58 MPa, and yield strength (YS) fell from 155 to 41 MPa during the test from 450 to 850 °C. After high-temperature tensile strength, the creep performance of the P92/304L dissimilar weld joint has also been investigated at 650 °C in the stress range of 100-200 MPa. All the creep specimens failed from the P92 steel parent metal region during the creep test at different conditions. The maximum creep life of 706.9 h was observed for the specimen tested at 650 °C under 100 MPa. The minimum creep life of 11.9 h was observed for the specimen tested at 650 °C under 200 MPa. The relationship between the rupture time and applied stress followed the logarithmic equation as log (t_r) = log (14.39695) + (− 5.79039) log (σ). The softening of the parent metal matrix due to the consumption of the solid solution strengthening W and Cr elements and the coarsening of the precipitates were the main reasons behind the creep failure at 650 °C in the stress range of 100-130 MPa. The plastic deformation caused by the grain boundary sliding was mainly responsible for creep failure at 650 °C in the stress range of 150-200 MPa.

Gaurav Dak, Abir Bhattacharyya, and Chandan Pandey, Indian Institute of Technology Jodhpur, Karwar, Rajasthan 342037, India; Krishna Guguloth, CSIR-National Metallurgical Laboratory, Jamshedpur, Jharkhand 831007, India; Pradeep Kumar, Indian Institute of Technology, Roorkee, Uttarakhand 247667, India. Contact e-mails: krishna@nmlindia.org and chandanpy.1989@gmail.com.

Graphical Abstract

Extraction of the creep and high-temperature tensile specimen from DMW joint of P92 and AISI 304L steel

High-temperature tensile results

Fractured creep specimen

Plot of creep strain as a function of time conducted at 650°C under the stress range of 150 200MPa and 100-140MPa

Plot of rupture time against the applied stress at 650°C

Creep rate vs. time plot to distinguish minimum creep rate (MCR) with respect to the applied stress

Plot of applied stress against LMP at 650°C

1. Introduction

The continuously rising demand for energy across the world urges scientists to develop highly efficient thermal power plants. New generation power plants, such as ultra-supercritical (USC), operate at high temperatures and pressure. These power plants are highly efficient compared to the previously developed subcritical and supercritical power plants because of their high operating parameters (temperature and pressure) and low coal consumption (Ref 1). The maximum working temperature and pressure of the thermal power plants are limited by the material that can operate at these conditions without failure. The CSEF steel (such as P92, P91, and P22), nickel-based super-alloys (such as Inconel 617, Inconel 800, and Inconel 625), and austenitic stainless steel (such as 304L and 304H) are regularly used material for high-temperature application in modern thermal power plants. The costly austenitic stainless steel is used in the high-temperature sections in the final stages of the superheater and reheater, where the main requirements are high creep strength and excellent oxidation resistance. The CSEF P92 steel is the most suitable material for constructing the header, boiler tubes, and steam generator of thermal power plants. According to the data provided by the International Energy Agency (IEA), the superheater tubes made from this steel operate at high steam temperatures and pressure (580-620 °C, 22-25 MPa) in USC power plants (Ref 2). From the economic viewpoint, the P92 steel is used at various locations of thermal power plants to utilize its ability to operate at high-temperature. The less expensive CSEF steel is employed in the low-temperature sections, in the primary boiler and heat exchangers. The bimetallic metal joint between an SS and CSEF steel is used widely in power plants to meet the design requirement and reduce the overall cost. However, premature failure in service has been reported for these bimetallic metal joints prepared with the iron-based filler metal within 1/3rd of

the designed service life. Thus, the better tri-metallic metal joint configuration of CSEF steel/Inconel 625/SS is discussed in this study (Ref 3). In power plants, connections must be made between various components made from different grades of steel, nickel-based super-alloy, or any other metals to meet the operating condition criteria and minimize the material cost. Among the various welding processes available, the GTAW process with suitable filler metal is most frequently used to make dissimilar tube-to-tube weld joints in power plants. The welded structure is commonly used in thermal and nuclear power plants due to its high strength, ease of repair, and design flexibility (Ref 4, 5). The GTAW is the most commonly used welding technique owing to its productivity, quality, and consistency and could be used to join P92 and 304L dissimilar metals (Ref 6). However, from the detailed literature review, it was concluded that further investigation is still required to fully understand the microstructural changes in the base metal near the fusion line and their impact on the overall creep behavior of welded components. The creep failure can be observed from the weld fusion zone if a filler metal with low creep and high-temperature strength compared to the parent metal is selected. The Inconel 625, Inconel 617, and Inconel 82 filler metals are regularly used to prepare such tri-metallic metal joints (Ref 7-9). However, the formation of the heat-affected zone (HAZ) due to the welding-induced heat is the most problematic region, as after long-term service, failure has been reported by many researchers from the HAZ of the CSEF steel (Ref 10).

The components in the USC power plants are subjected to very high temperatures (570-650 °C) and pressure (25-30 MPa). Thus, it is essential to investigate the stability of these dissimilar weld joints at elevated temperatures (Ref 11). The mechanical and microstructural properties of the P92 steel and 304L at elevated temperature decide the reliability of these dissimilar weld joints for power plant application. The 304L, 304H austenitic steel is comparatively more stable at high temperature than P92 CSEF steel due to the high amount of the nickel (Ni) and chromium (Cr) elements in its chemical composition. To guarantee the long-term safety and reliable operation of thermal power units in high-temperature environments, it becomes imperative to thoroughly investigate the high-temperature tensile properties and creep resistance of these dissimilar weld joints. The failure of such joints due to the degradation of the microstructure before the predicted service life has been reported in the literature (Ref 12). The ferritic steel primarily influences the creep rupture behaviors of dissimilar weld joints involving ferritic and austenitic steels, as it exhibits relatively inferior creep strength compared to the austenitic steel. In the case of creep condition, the ruptures typically occur from one of the following locations: the parent metal of the ferritic steel (Ref 13), the HAZ of the ferritic steel (Ref 14), or at the weld fusion zone and the ferritic steel interface (Ref 15). These identified areas are critical points where failures happen due to the stresses and operating conditions experienced during creep deformation. The superheater tubes made from the P92 steel are exposed to fireside corrosion, steam side oxidation, static load, and fluctuating thermal gradients, which cause creep damage. Thus, it is vital to investigate the creep performance of these tri-metallic metal joints. The microstructure degradation of the P92 steel at elevated temperature is the foremost limiting factor for continuously using this tri-metallic metal joint at higher temperature (Ref 16, 17). The main reason behind the failure was the coarsening of the precipitates and the development of the laves phase and Z phases. The heterogeneous

microstructure developed across the P92 steel side deteriorates the creep rupture strength of the P92 steel. The softening of the P92 steel at high temperatures due to the destabilization of the tempered martensite results in Type IV (failure from the fine grain heat-affected zone (FGHAZ) or inter-critical heat-affected zone (ICHAZ)) failure. Thus, it is essential to determine the creep life and high-temperature tensile performance of these dissimilar weld joints (Ref 18, 19). The addition of the cobalt (Co) element in the P92 steel improves the creep strength by reducing the prior austenite grain size and tempered martensite lath size (Ref 20). Sakthivel et al. (Ref 21) observed the creep failure from the P92 steel parent metal during the high-stress condition and the P92 HAZ region during the low-stress condition. The failure from the P92 steel parent metal and HAZ region is due to the rapid microstructural changes at elevated temperature service (Ref 22). Miao et al. (Ref 19) observed the Type IV cracking for the TP347H/T91 dissimilar steel weld joint prepared using ERNiCr-3 filler metal. Xue et al. (Ref 23) pointed out that type IV cracking occurs under higher stress and low-temperature condition. Huang et al. (Ref 24) reported the rupture of the P92 steel parent metal under creep test at 625 °C and 250 MPa. The creep fracture mechanism of T92/HR3C dissimilar weld joint under creep condition of 650 °C and with lower applied stress of 90 MPa was examined by Wang et al. (Ref 25). The dissimilar weld joint was created utilizing the GTAW technique and Inconel 82 Ni-based filler. The result showed the creep failure from the P92 FGHAZ region. Liu et al. (Ref 26) reported that the stress concentration created by the coarse carbide precipitates, triple boundary and matrix softening is the main reason behind the formation of the creep cavity. The literature review indicated that the creep rupture location depends on the applied stress and temperature. This research article provides a detailed discussion regarding the microstructure changes in the P92 HAZ region and near the necking surface after specimen failure. The detailed information regarding the microstructure evolution and mechanical properties after the high-temperature tensile and creep service of this combination (P92-ERNiCrMo-3-304L) of the dissimilar weld joints is still unavailable in the public domain. Therefore, this study discusses a detailed investigation of the mechanical and microstructural properties after the creep and high-temperature tensile test of the P92-ERNiCrMo-3-304L dissimilar weld joint. It should be noted that in this research article, the high-temperature tensile and creep test was performed after the welding and without any further post-weld heat treatment. In addition to the microstructural investigation, micro-hardness measurement was performed along the cross section of the ruptured specimen.

2. Materials and Experimental Procedure

The P92 CSEF steel and 304L SS were chosen as parent metals to prepare the dissimilar weld joint by the fusion welding process. The ERNiCrMo-3 (Inconel 625) was chosen as filler metal due to its excellent mechanical and microstructural properties at elevated temperatures. The chemical composition of the parent material and ERNiCrMo-3 filler metal used in the present investigation is available in our previous work (Ref 27). Also, the detailed welding procedure, welding parameters, macro- and microstructure examination, micro-hardness distribution, mechanical property investigation, and

residual stress analysis of V-groove geometry P92/304L dissimilar weld joint are provided in our previous work (Ref 27, 28). For the preparation of the high-temperature tensile and creep specimen, the rectangular strip was taken from the transverse direction of the dissimilar weld joints, as shown in Fig. 1. The round shape high-temperature tensile and creep specimens of required dimension, as shown in Fig. 2(a)-(b), were then prepared using a lathe machine. The cylindrical shape specimen for the high-temperature tensile test with a 3 mm diameter, gauge length of 70 mm, and gripping length of 20 mm was prepared from the transverse direction of the weld according to the ASTM E8 standard. The high-temperature tensile test was conducted using a hydraulic universal testing machine (Make: Shimadzu) of 50 kN capacity. The test was performed at a strain rate of 0.001 s^{-1} and 0.5 mm/min loading rate. Specimens for the creep tests were prepared following the standard specification (ASTM E139), having a diameter of 6 mm and a gauge length of 33 mm. Constant load creep tests have been conducted at 650 °C within the stress range of 100-200 MPa. Tests were performed using the Mayes machines having 30 kN loading capacity. Two thermocouples were used within the gauge portion of the specimen to measure the testing temperature and controlled within ± 3 °C. The strain was measured continuously till the failure of a specimen as a function of time from the extensometer connected in the gauge section and linear variable differential transducer (LVDT) assembly.

For metallographic investigation, the fractured tensile specimen was sliced into two halves from the transverse direction of the weld. The extracted sample was then hot-mounted with epoxy resin for further metallographic procedure. The hot-mounted specimen of dimension 30 mm was then mirror polished using SiC abrasive paper from #80 grit to #2000 and 1 μm alumina slurry. The dissimilar weld joint consists of three different metals, so three different chemical etchants were used to reveal the microstructure features. The P92 metal surface was chemically etched using Villella solution [1 g picric acid ($C_6H_3N_3O_7$) + 5 ml hydrochloric acid (HCL) + 100 ml of ethanol (C_2H_6O), 35 s], and 304L using aqua regia (HNO_3 + HCL, 1:3, 20 s) solution. The ERNiCrMo-3 weld metal was electrolytically etched at a voltage of 4 V for the 30 s in a 10 wt.% oxalic acid solution.

3. Results and Discussion

3.1 High-Temperature Tensile Test

The high-temperature tensile test was conducted at different temperatures to determine the YS and UTS values of the P92-ERNiCrMo-3-304L dissimilar weld joint at different temperatures. The high-temperature tensile strength test was conducted at an interval of 100 °C within the temperature range of 450-850 °C. The tensile strength of the 588 MPa was observed at room temperature, and decreased to 47 MPa at 850 °C. The UTS and YS value decreased with the increase in the test temperature. During the room temperature tensile test, the specimen failed from the 304L parent metal due to the low UTS and YS value of the 304L steel than P92 steel and ERNiCrMo-3 weld metal at room temperature (Ref 27). The dissimilar weld joint failed from the 304L parent metal up to the temperature of 550 °C. The fracture location shifted from the 304L parent metal at 450 and 550 °C to the P92 steel parent metal at 650, 750, and 850 °C. Thus, the mechanical and microstructural properties of the P92 steel degrade quickly after the maximum operating temperature range. Although the test was carried out
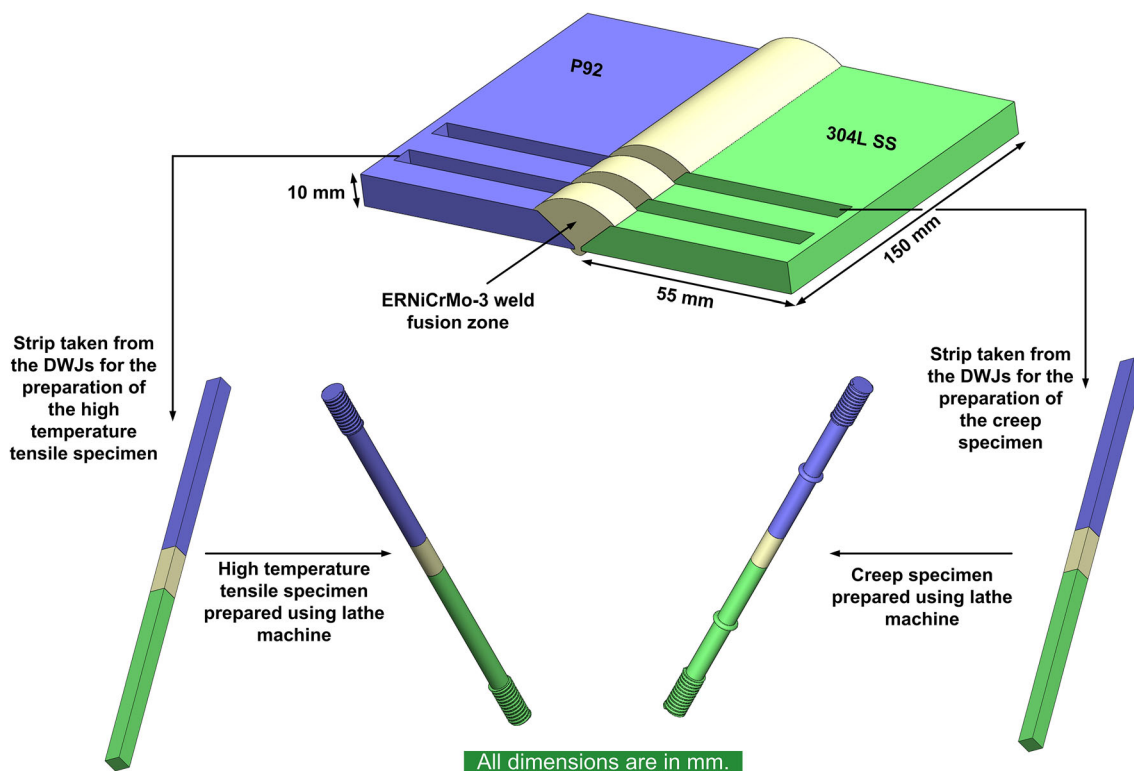

Fig. 1 Schematic diagram of the dissimilar weld joint, creep and high-temperature tensile test specimen preparation
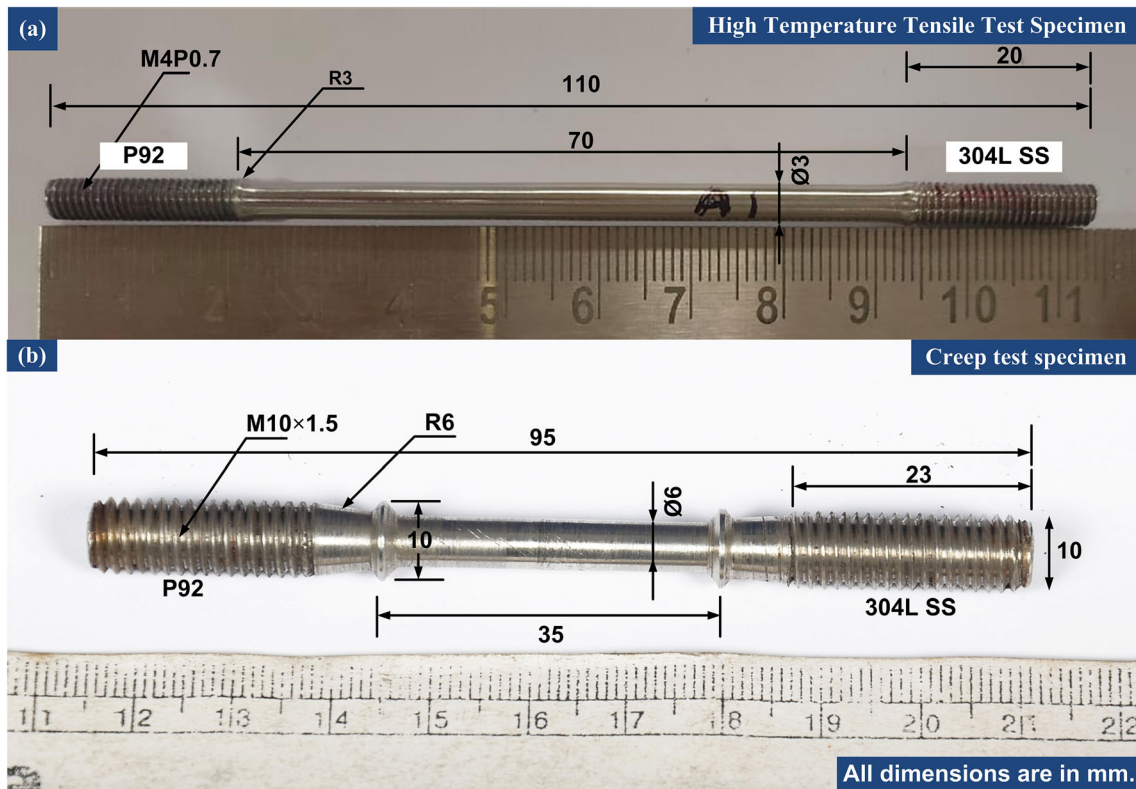
Fig. 2 (a) High-temperature tensile test specimen and (b) Creep test specimen

up to 850 °C, the weld metal did not crack. This indicates the excellent stability of the ERNiCrMo-3 filler metal at elevated temperature service. Figure 3(a)-(e) shows the appearance of the ruptured high-temperature tensile specimen. It becomes difficult to determine whether a fracture originated from the HAZ or parent metal if it occurs close to the weld interface. However, as in present case the fracture location was far away from the weld interface, the exact fracture location was easy to identify.

The stress–strain curve obtained at room and elevated temperature is shown in Fig. 4(a). The variation in the UTS value, YS value, % elongation, and % reduction in cross-sectional area with respect to test temperature is shown in Fig. 4(b)-(c). The stress–strain curve indicated the serrated flow/jerky flow behavior during the plastic deformation for the high-temperature test. The strain aging process hardens the material. Thus, the stress required to deform the material increases after strain/work hardening. Strain aging can also occur during plastic deformation; in that case, it is called dynamic strain aging (DSA). DSA occurs at a particular temperature and strain rate. DSA is an unwanted phenomenon as it decreases the ductility and toughness of the material. DSA occurs due to the pinning of the dislocations by solute atoms. This phenomenon is also called serrated flow behavior, as the stress–strain curve exhibits serration during the plastic defor-mation. DSA results from the interaction between dislocations and solute atoms during plastic deformation. When dislocations encounter impediments during plastic deformation, they are momentarily halted. As the solute atoms diffuse around the pinned dislocations during this period, the hold of the barrier on the dislocations is further strengthened. With enough tension, these dislocations eventually pass the obstacles and proceed to

the next one where they are stopped, allowing the process to continue. This interaction will result in the inhomogeneous deformation behavior, called serration in the stress–strain curve, as seen from the stress–strain curve at 450 and 550 °C. The serrated flow occurs due to the locking and releasing of the dislocations by the solute atom, which results in the jerky flow during the high-temperature tension test (Ref 29). The Portevin and Le-Chatelier developed this theory of serration, hence also called the Portevin Le–Chatelier (PLC) effect. There are three types of serration behavior depending on the profile of the stress–strain curve: Type A, Type B, and Type C. The serration type varies with the temperature and strain rate (Ref 30). According to results in the literature, DSA mostly happens in 304L (Ref 31, 32). Also, the DSA happens at a specific strain rate and temperature (Ref 30). DSA primarily happens in alloys with interstitial solute atoms because these atoms can quickly and forcefully segregate to dislocations and lock them during straining. At elevated temperatures and low strain rates, the mobility of solute atoms in this steel increases to the point that they can follow a dislocation during its motion and segregate to its core while it has to wait in front of an obstacle. DSA happens when the repeated interaction of interstitial solute atoms prevents dislocation motion. Serrations or wavy patterns resembling saw teeth in the stress–strain plot are seen in this situation. Most studies have shown that the serrated flow is suppressed with increase in strain rate and decrease in temperature (Ref 33). The room temperature and elevated temperature UTS value, YS value, % elongation, and % reduction in cross-sectional area of the P92 and 304L dissimilar weld joints prepared using ERNiCrMo-3 filler are listed in Table 1. From the high-temperature tensile test results, it was noticed that as the test temperature increases, the time to failure
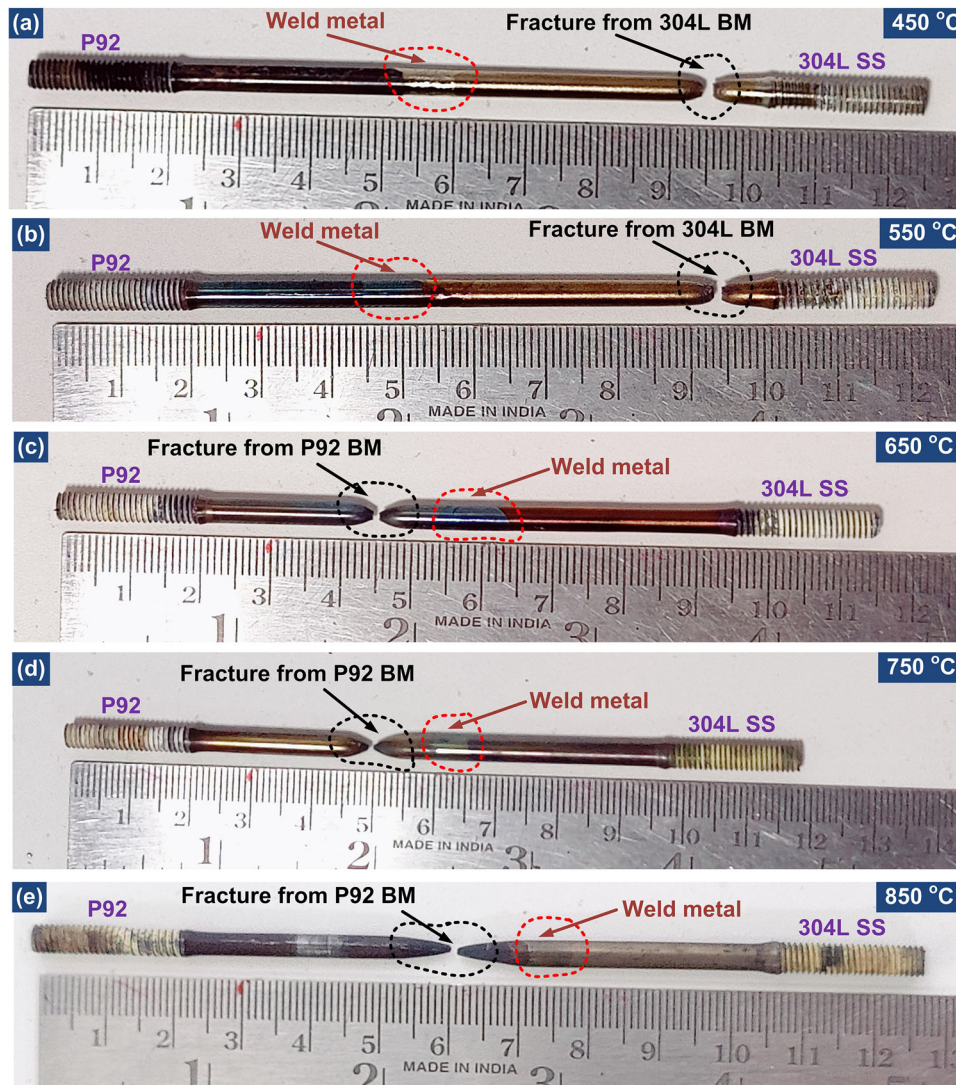
Fig. 3 (a-e) Photograph of the ruptured high-temperature tensile specimen, showing the fracture location at different test temperature

of the P92/304L dissimilar weld joint decreases. The metallurgical changes toward the specimen failed from the 304L and P92 side were examined by taking the cross section of the fracture surface.

3.2 Macrostructure of the Fractured High-Temperature Tensile Test Specimens

Figure 5(a)-(e) shows the macrograph of the cross section of the fractured high-temperature tensile test specimen. The macrograph shows the fracture specimen consisting of P92 parent metal, 304L parent metal, ERNiCrMo-3 weld metal, P92 HAZ, and 304L HAZ in gauge length. P92 steel has excellent strength at low temperature compared to the 304L. Therefore, the specimen tested at 450 and 550 °C was fractured from the 304L parent metal. As the test temperature increases, the strength of the P92 steel falls rapidly due to the changes in the metallographic structure. Thus, the specimen tested at 650, 750, and 850 °C was fractured from the P92 steel parent metal. From the above observation, it can be said that up to 550 °C, P92 steel has a higher UTS value than 304L. However, the UTS value of the P92 steel degrades quickly after its maximum designed operating temperature. The macrographs showed no

significant deformation in the weld metal structure after the high-temperature tensile test. The weld fusion zone was free from cracking and deformation for all the test temperature. This indicates the reliability of the nickel-based filler metal for elevated temperature service.

3.3 Microstructure Changes After High-Temperature Tensile Test

The major microstructural variation was observed near the fracture tip surface. The specimen tested at 450 and 550 °C failed from the 304L parent metal. The microstructure near the fracture region of these high-temperature tensile specimens is shown in Fig. 6(a)-(f). The as-received 304L austenitic stainless steel primarily consists of austenite grains, twins, and ferrite stringers, as already discussed in our previous work (Ref 27, 28). The 304L is a non-heat treatable alloy. Thus, it does not undergo any phase transformation or microstructural evolution at elevated temperature service. It undergoes only strain/work hardening during plastic deformation at elevated temperature. The austenite grains and twins were stretched during the elevated temperature tensile test. Thus, the specimen tested at 450 and 550 °C and fractured from the 304L does not contain
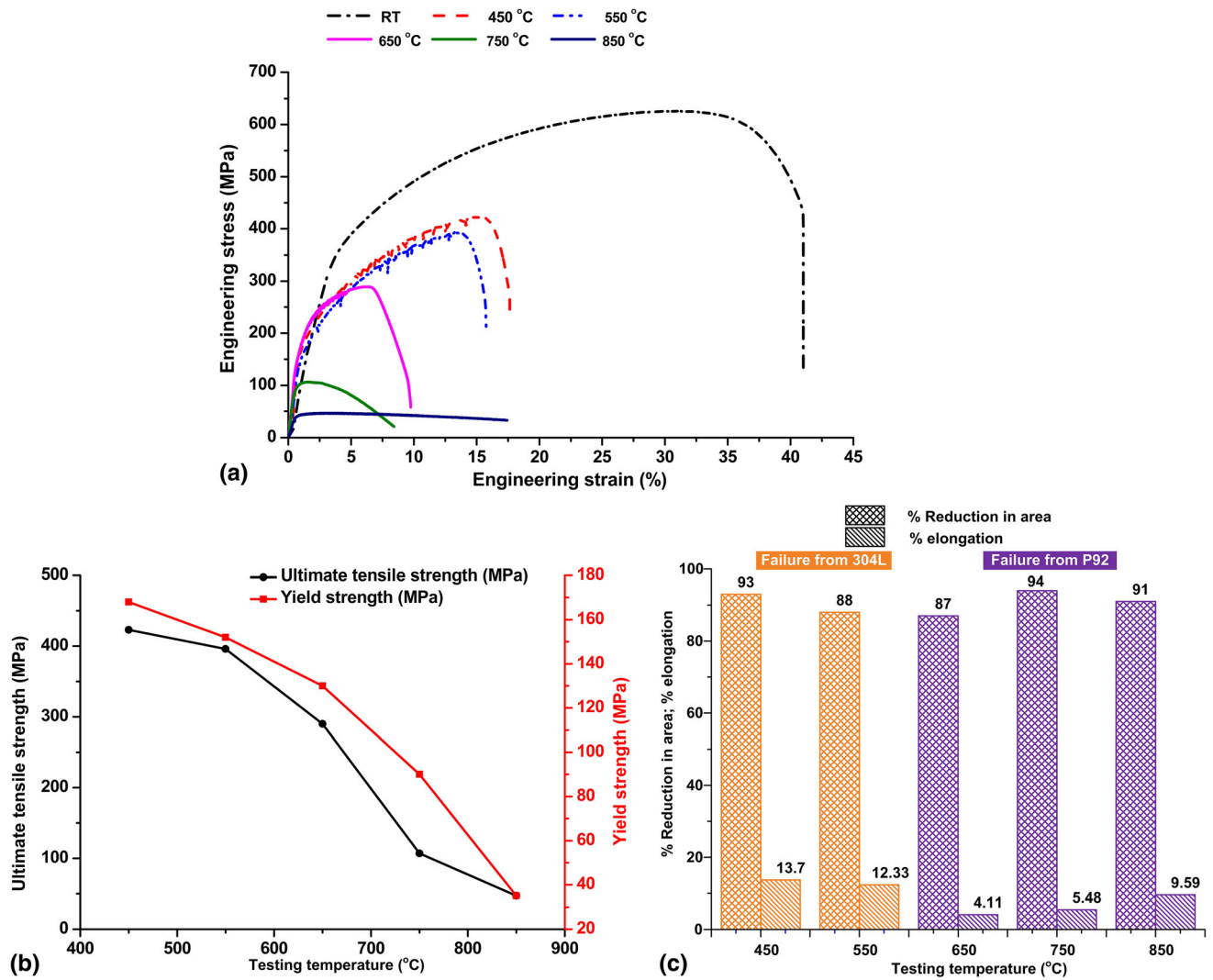
Fig. 4 (a) Engineering stress–strain curve at room and elevated temperature (450-850 °C), serrated flow behavior can be observed from the curve at 450 and 550 °C temperature, (b) relationship between test temperature and ultimate tensile strength and yield strength, and (c) relationship between test temperature and % elongation and % reduction in area

Table 1 Room temperature and high-temperature tensile strength of the P92-ERNiCrMo-3-304L dissimilar weld joint

Temperature, °C	Ultimate tensile strength, MPa	Yield strength, MPa	% Elongation	% Reduction in cross-sectional area	Fracture location
25, Room temperature	588	375	31	…	304L parent metal/base metal (BM)
450	423	168	13.7	93	304L parent metal
550	396	152	12.33	88	304L parent metal
650	290	130	4.11	87	P92 parent metal
750	107	90	5.48	94	P92 parent metal
850	47	35	9.59	91	P92 parent metal

twins and austenite grains in its microstructure, as shown in Fig. 6(a)-(f). The elongated ferrite stringers were only observed after the high-temperature tensile test. Song et al. (Ref 34) also observed similar microstructure characteristics for the HR3C advanced austenitic steel after the high-temperature tensile test. The microstructure of the specimen tested at 650, 750, and 850 °C, and fractured from the P92 steel parent metal is shown

in Fig. 7(a)-(i). The microstructural observation near the fracture surface showed the absence of the lath martensite structure and prior austenite grains. The precipitate (possibly $M_{23}C_6$ and MX type) of different sizes was observed near the fracture surface. Also, very few grain boundaries were observed near the fracture tip surface. Many cavity formations near the necking region indicate that the specimen has undergone a
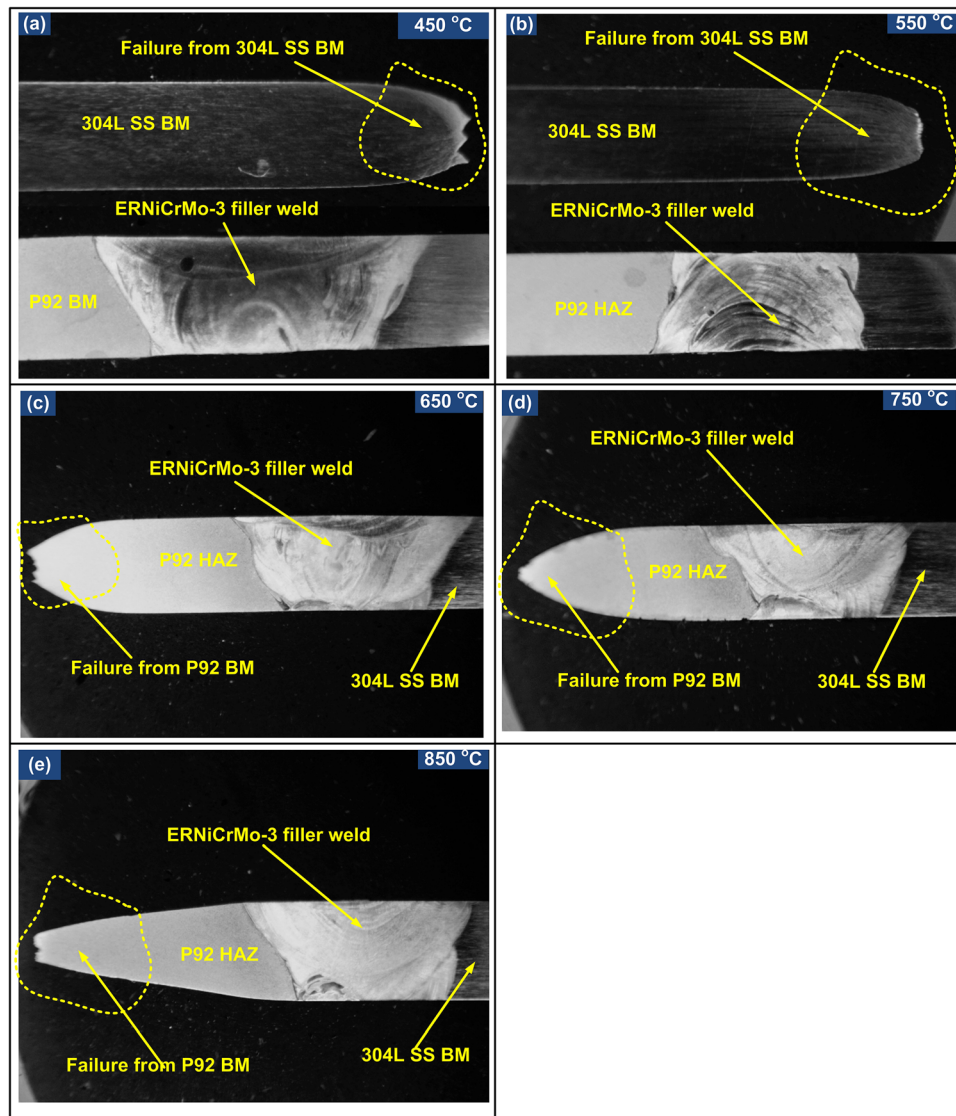
Fig. 5 (a-b) showing macrostructure of the tensile tested sample at 450 and 550 °C, which was taken from the localized portion of the 304L parent metal sample and (c-e) showing macrostructure of the tensile tested sample at 650, 750, and 850 °C, which was taken from the localized portion of the P92 parent metal sample

significant plastic deformation before fracture. The plastic deformation causes the softening of the matrix. Thus, this region becomes weaker during the tensile test and decreases the tensile strength. Small cracks and voids were formed near the necking surface. Crack formation and crack propagation are the two main steps of fracture. The slow crack propagation leads to ductile fracture, while the rapid crack propagation leads to brittle fracture. The tension load will create the necking at the low-strength region. As time passes, small micro-void formation occurs at the necking region. In the later stage, the coalescence of the micro-voids takes place. In this stage, the micro-voids become sufficiently large to form a crack. The number of cavities near the fracture tip surface increased with the increase in the test temperature, as shown in Fig. 7(a), (d), and (g). No crack or cavity was observed at the surface away from the necking region, as seen from the weld interface image (Fig. 7c). It should be noted that fewer voids were observed in the coarse grain heat-affected zone (CGHAZ) and FGHAZ regions, indicating the less effect of the applied load and

temperature on the microstructural properties of the P92 HAZ region. Also, the specimen tested at 650, 750, and 850 °C showed good necking before fracture. The specimen was tested at 650, 750, and 850 °C, which is an approximate tempering temperature for P92 steel. Thus, the microstructure of this region was slightly tempered after the high-temperature tensile test, and the tempered martensite structure of CGHAZ and FGHAZ region is shown in Fig. 7(f).

The mechanical properties are linked with the microstructure of the material. The FESEM microstructure of the specimen prepared from the cross section of the fractured high-temperature tensile specimen near the fracture tip surface is shown in Fig. 8(a)-(i). The maximum working temperature of the P92 steel is 620-625 °C (Ref 35). The test at 650-850 °C showed the failure from the P92 parent metal. Under elevated temperature tensile test, elongated grain boundaries were observed near the fracture tip surface. The grain boundaries are elongated due to the high tensile load applied at elevated temperature. The numerous voids that occurred around the prior
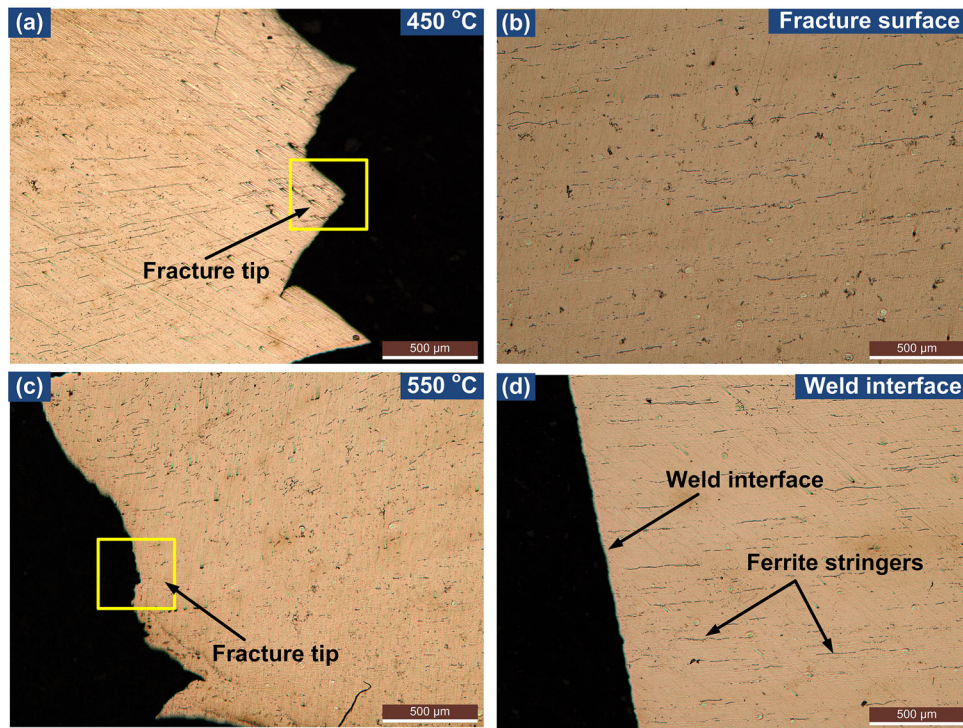
Fig. 6 (a) Optical microstructure of the fracture tensile specimen at 450 °C: fracture region, (b) microstructure near the fracture tip surface, (c) optical microstructure of the fracture tensile specimen at 550 °C: fracture surface, and (d) microstructure at the weld interface

austenite grain boundaries after the high-temperature tensile test are shown in Fig. 8(a)-(i). The cavity formation occurs mainly along the triple point of the prior austenite grain boundaries (Ref 36), as shown in Fig. 8(b), (e), and (h). The large numbers of voids that occur near the fracture surface coalesce together and form cracks. From the elevated temperature tensile test results, it is clear that the P92 steel softens more rapidly than the 304L steel with increase in temperature. During the high-temperature tensile test, the growth of the $M_{23}C_6$ precipitates in the P92 steel increases, resulting in the loss of the precipitation-strengthening effect due to the segregation of the important Cr and Ni elements from the base metal matrix. The energy-dispersive-spectroscopy (EDS) point analysis was conducted near the fracture tip surface containing coarse and fine secondary phase particles around the cavity. The EDS spectrum result was C: 7.82%, Cr: 8.98%, Fe: 75.86%, Nb: 3.72%, W: 2.28%, Mo: 1.08%, Ni: 0.33%. The result indicated that the $M_{23}C_6$ precipitates near the cavity. The W element presents in the $M_{23}C_6$ precipitates retard the coarsening rate of these particles. At high temperature, carbide-forming elements such as Cr and C from the matrix diffuse into the $M_{23}C_6$ precipitates, hence increasing the coarsening of these particles (Ref 37). The grain boundaries decorated with the $M_{23}C_6$ precipitates mainly obstruct the dislocation movement under applied tension load. At high temperature, because of the coarsening of the $M_{23}C_6$ precipitates, the pinning effect provided by these precipitates gets suppressed. Thus, at high-temperature, failure takes place from the P92 steel. The coarsening and cluster of the $M_{23}C_6$ precipitates during the high temperature are the main reasons behind the reduction of the P92 steel strength at high temperature. The laves phase was not observed after the high-temperature tensile test.

3.4 Micro-hardness Distribution After High-Temperature Tensile Test

The Vickers micro-hardness test was conducted over the same specimen used for microstructural characterization consisting of the necking region, P92 HAZ, P92 parent metal, IN 625 weld metal, 304L parent metal, and 304L HAZ. The indentations were taken at a regular interval of 0.25 mm by applying a load of 500 gf for 10 s. The Vickers micro-hardness distribution across the cross section of the fracture high-temperature tensile test specimen is presented in Fig. 9(a)-(e). The micro-hardness across the P92/304L dissimilar weld joint after welding is presented in our previous work (Ref 27). The micro-hardness value obtained after welding was also taken into consideration to approximate the fracture location. For all the specimens, the fracture point was selected as the starting point for the hardness measurement (X = 0). The cross section of the fractured tensile test specimen was divided into three parts: fracture point and corresponding parent metal, weld metal, and un-affected parent metal. Based on the micro-hardness distribution, the fracture location can be estimated. The micro-hardness variation at each point also shows the extensive microstructural evolution as well as microstructural inhomogeneity after tensile testing at different temperatures. The specimen tested at 450 and 550 °C failed from the 304L parent metal. From the micro-hardness data across the 304L region after the high-temperature tensile test, it was pointed out that the hardness of the 304L was higher than that of the as-received 304L. The maximum micro-hardness of the 304L increased to 310 HV near the fracture point after the high-temperature tensile test. The increase in the micro-hardness value of the 304L after the high-temperature tensile test is due
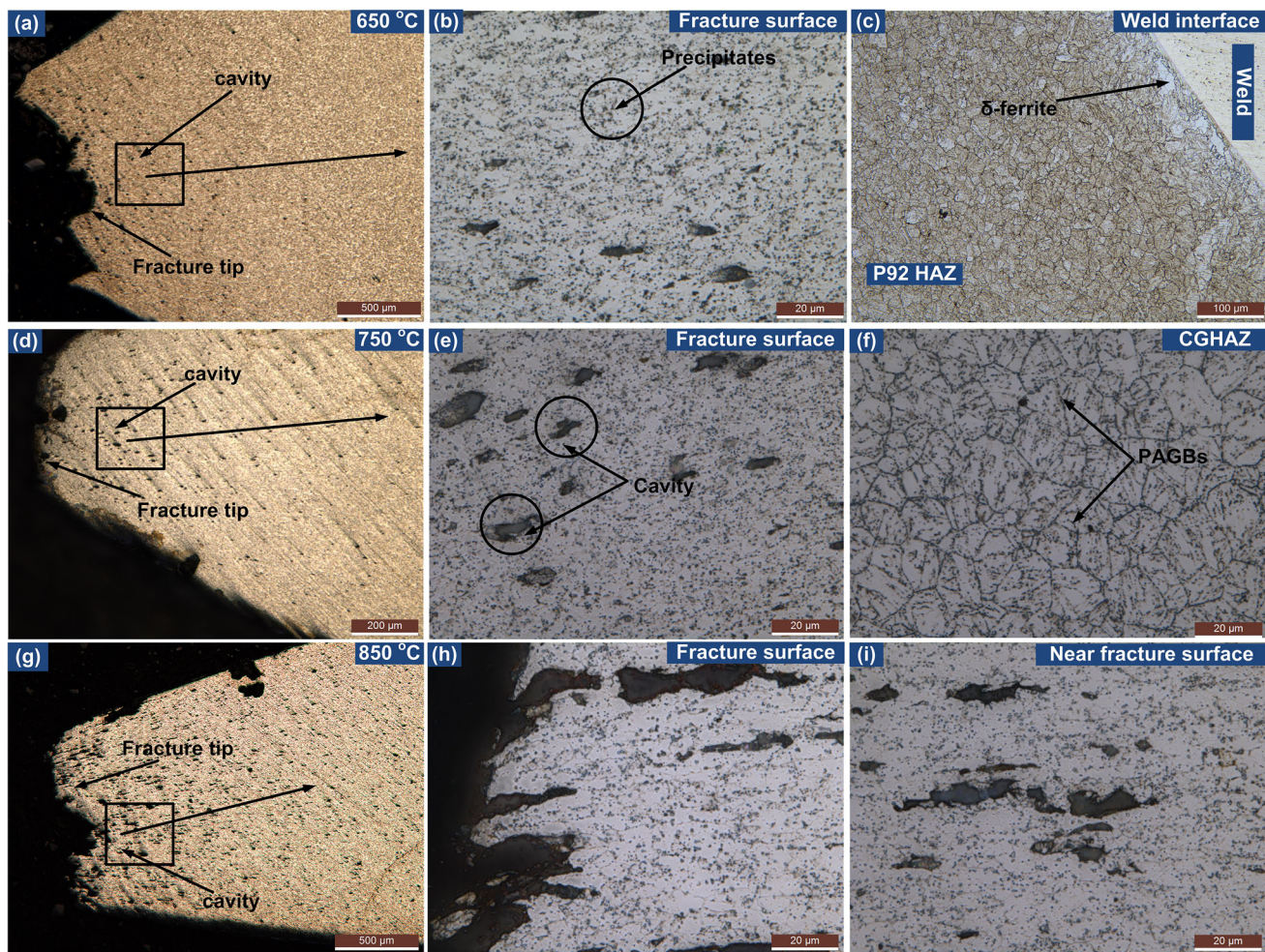
Fig. 7 Optical microstructure of the tensile tested specimen till fracture; consisting of fracture region, micro- and macro-voids can be observed (a) optical microstructure of the fracture tensile specimen tested at 650 °C, (b) microstructure of the fracture region, (c) microstructure at the weld and P92 HAZ interface, (d) optical microstructure of the fracture tensile specimen tested at 750 °C, (e) microstructure near the zone of failure, (f) microstructure of the P92 CGHAZ region, (g) optical microstructure of the fracture tensile specimen at 850 °C, (h) microstructures of the fracture region and (i) microstructure near the fracture region

to the work hardening or strain hardening effect (Ref 38). The DSA phenomenon discussed in the previous section is mainly responsible for the increase in the hardness value of the 304L after the high-temperature tensile test. The DSA is a consequence of plastic deformation. The 304L austenitic stainless steel is a non-heat treatable and ductile metal. Thus, during the plastic deformation, because of the increase in the number density of the dislocation, the hardness of the 304L steel increases. It can be pointed out from the micro-hardness distribution that the micro-hardness near the fracture tip surface was changed dramatically for all the test temperature due to the microstructure changes. From the micro-hardness across the necking surface, it can be confirmed that failure took place from the P92 parent metal for the specimen tested at 650-850 °C. The low micro-hardness value was observed in the rupture location of the P92 steel (as low as 90 HV for the specimen tested at 850 °C). The extremely low micro-hardness value at the fracture tip surface was due to the extensive plastic deformation that occurred in the P92 steel and thus large numbers of voids formation. It was observed that as the tensile test temperature increases, the hardness value of the P92 steel decreases at the fracture location. It should be noted that the

hardness of the P92 steel near the fracture region (for the specimen tested at 650-850 °C, and failed from the P92 base metal) decreased noticeably after the high-temperature tensile test. The reason why P92 steel shows a low micro-hardness value after a high-temperature tensile test is because of the softening of the lath martensite structure and the coarsening of the precipitates at elevated temperatures. Also, the degradation of the martensite lath structure and the decrease in the dislocation density are mainly responsible for a drop in the micro-hardness value of the P92 steel after the high-temperature tensile test. The hardness value across the P92 HAZ decreases considerably with an increase in the test temperature due to the tempering effect once the high-temperature tensile test is completed. The hardness value of the CGHAZ and ICHAZ region vary significantly for each test specimen after a high-temperature tensile test at different temperature due to the heating at various temperatures (450-850 °C) and then cooling after a fracture. The hardness gradient for the nickel-based weld metal was smaller for the different high-temperature tensile test temperature. It shows the good stability of the nickel-based filler metal at elevated temperature.
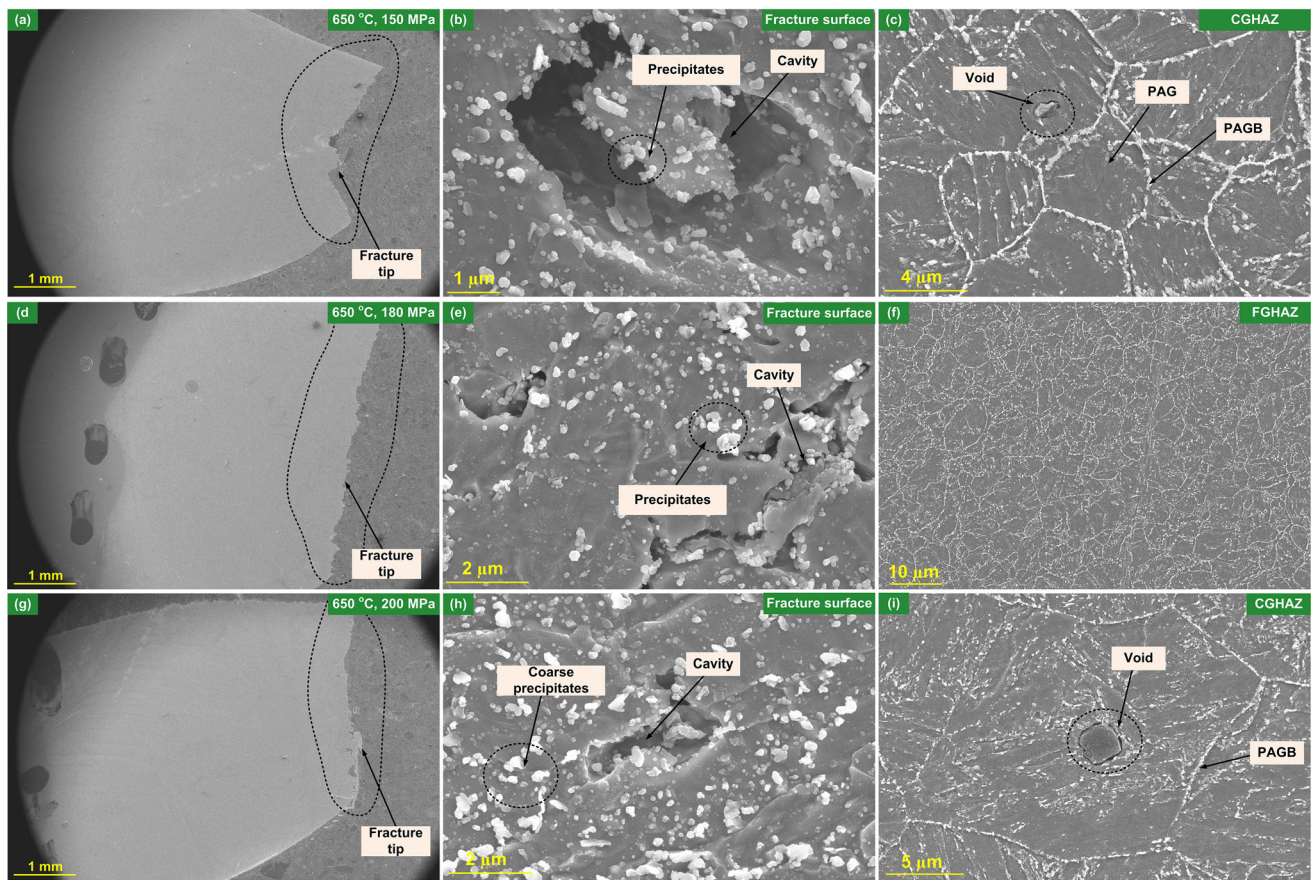
Fig. 8 (a) FESEM microstructure of the fracture tensile specimen tested at 650 °C: fracture surface, (b-c) microstructure near the fracture region at low and high magnification, (d) FESEM microstructure of the fracture tensile specimen tested at 750 °C: fracture surface, (e-f) microstructure near the fracture region at low and high magnification, (g) FESEM microstructure of the fracture tensile specimen tested at 850 °C: fracture surface and (h-i) microstructure near the fracture region at low and high magnification

3.5 Fracture Surface Analysis of High-Temperature Tensile Specimens

The SEM microstructure of the fracture surface of the specimen at low (50X) and high magnification (1500X and 2500X) is shown in Fig. 10(a)-(e). The low-magnification image, as shown in Fig. 10(a)-(e), was used to measure the reduced diameter of the fractured high-temperature tensile specimen with the help of the SEM measurement tool. The low-magnification image also shows the overall appearance of the fracture surface. The magnified image of the specified region at high magnification is also shown in subsequent Figures. It should be noted that the P92/304L dissimilar weld joint was fractured from the 304L parent metal during the tensile test at 450 and 550 °C. The fracture surface of the 304L parent metal is shown in Fig. 10(a)-(b). From the low-magnification image of the specimen tested at 450 and 550 °C, it can be observed that the fracture surface contains few voids and dimples. The very small size micro-voids were observed from the high-magnification microstructure image. The flat fracture surface appearance was also observed near the voids and dimples. Thus, the ductile–brittle mode of the fracture occurred for the specimen that failed from the 304L parent metal. Also, due to the DSA phenomenon occurring in the 304L steel, the brittleness of the 304L material increases. This phenomenon is responsible for the brittle mode of the fracture from the 304L. The specimen was fractured from the P92 parent metal when tested at 650, 750, and 850 °C. The specimen ruptured from the P92 steel had a large necking, suggesting that the fracture was in plastic manner. The fracture surface of the P92 steel is shown in Fig. 10(c)-(e). The fracture surface of the elevated temperature tensile tested specimen mainly consists of dimples and voids of different sizes and shapes. Large voids were also observed at the surface of the fractured specimen with higher test temperature, i.e., 650-850 °C. From the microstructure of the fractured surface, it was observed that the microstructure at the center of the fractured surface and the edge was different. The comparatively larger voids were observed at the center region compared to the edge of the fractured surface. The large number of voids at the fracture surface indicates the high plastic deformation due to the applied stress. The small and large voids at the fracture surface indicate the ductile fracture. Chen et al. (Ref 17) also reported similar fracture modes. The authors reported small, shallow, and equiaxial dimples at low test temperature and large, deep, and completely parabolic dimples at elevated temperature. The type and size of dimples change with the change of the test temperature. From the fractography of the failed surface at different temperatures, it was observed that the number of dimples and voids increases as the test temperature increases. The fracture surface of the specimen tested at 850 °C, as shown in Fig. 10(e), it can be understood that the surface was completely oxidized at such a high temperature.
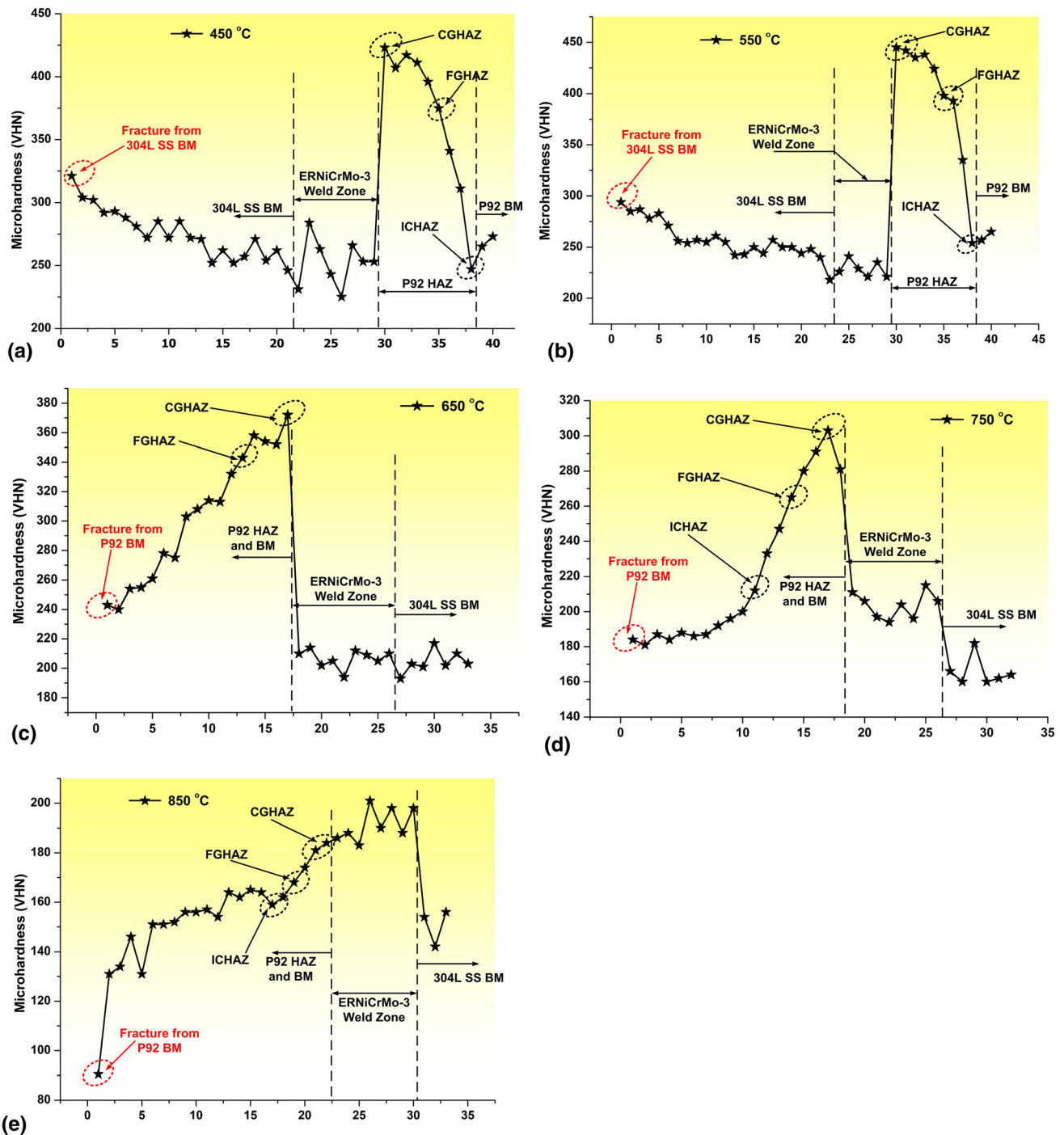
Fig. 9 (a-e) Micro-hardness profile across the tensile fractured specimens tested at various temperatures in the 450-850 °C range

4. Creep Test

The creep is an essential property for any material used at high temperature and stress condition. The creep properties of the P92/304L dissimilar weld joint were investigated at constant temperature and varying the applied stresses. The creep rupture tests were conducted at 650 °C with applied stress in the 100-200 MPa range. The rapid microstructural changes occur in the P92 steel after 650 °C. Thus, the operating temperature was selected as 650 °C to shorten the creep rupture time. The maximum creep rupture time was obtained for the

specimen tested at 650 °C under 100 MPa. At the same time, the minimum rupture time was obtained for the specimen tested at 650 °C under 200 MPa. Kim et al. (Ref 39) also observed the similar results for the T92/304H dissimilar weld joint prepared using ERNiCr-3 filler metal. The creep deformation was observed from the P92 parent metal and FGHAZ region, respectively. However, the creep test was performed after the post-weld heat treatment. Figure 11(a)-(e) shows the creep ruptured specimens of P92/304L dissimilar weld joint at 650 °C and applied stress of 100, 130, 150, 180, and 200 MPa. The fracture occurred from the P92 steel parent
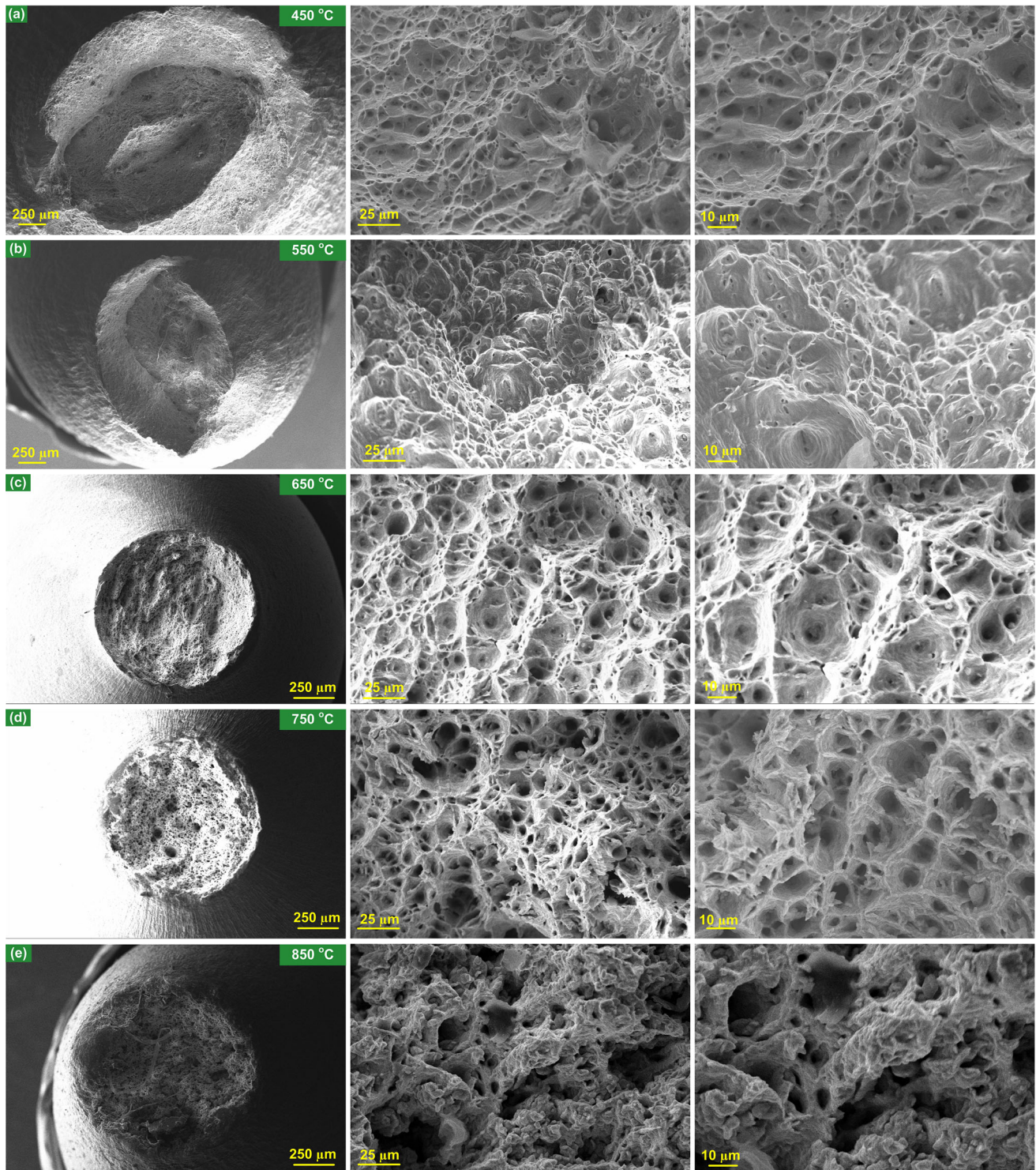
Fig. 10 (a-e) FESEM images were taken from the fracture surface of the high-temperature tensile tested specimen

metal. The IN625 filler weld fusion zone and 304L parent metal were safe after the creep test. The creep test results showed that the 304L and nickel-based filer have better creep strength and thermal stability than P92 steel.

4.1 Experimental Procedure and Results

Creep is a time-dependent phenomenon that occurs continuously during plastic deformation at constant stress. The creep test is conducted by placing a constant load on the test specimen, and change in strain is measured with respect to time at a constant temperature. Creep tests were performed as per the ASTM E139 standard (Ref 40). The creep curve of the various specimens tested under constant load at 650 °C is shown in Fig. 12(a), (b). The creep rupture lives of the P92/304L dissimilar weld joint depend on the test temperature and applied stress. The creep rupture time decreases with the increase in the
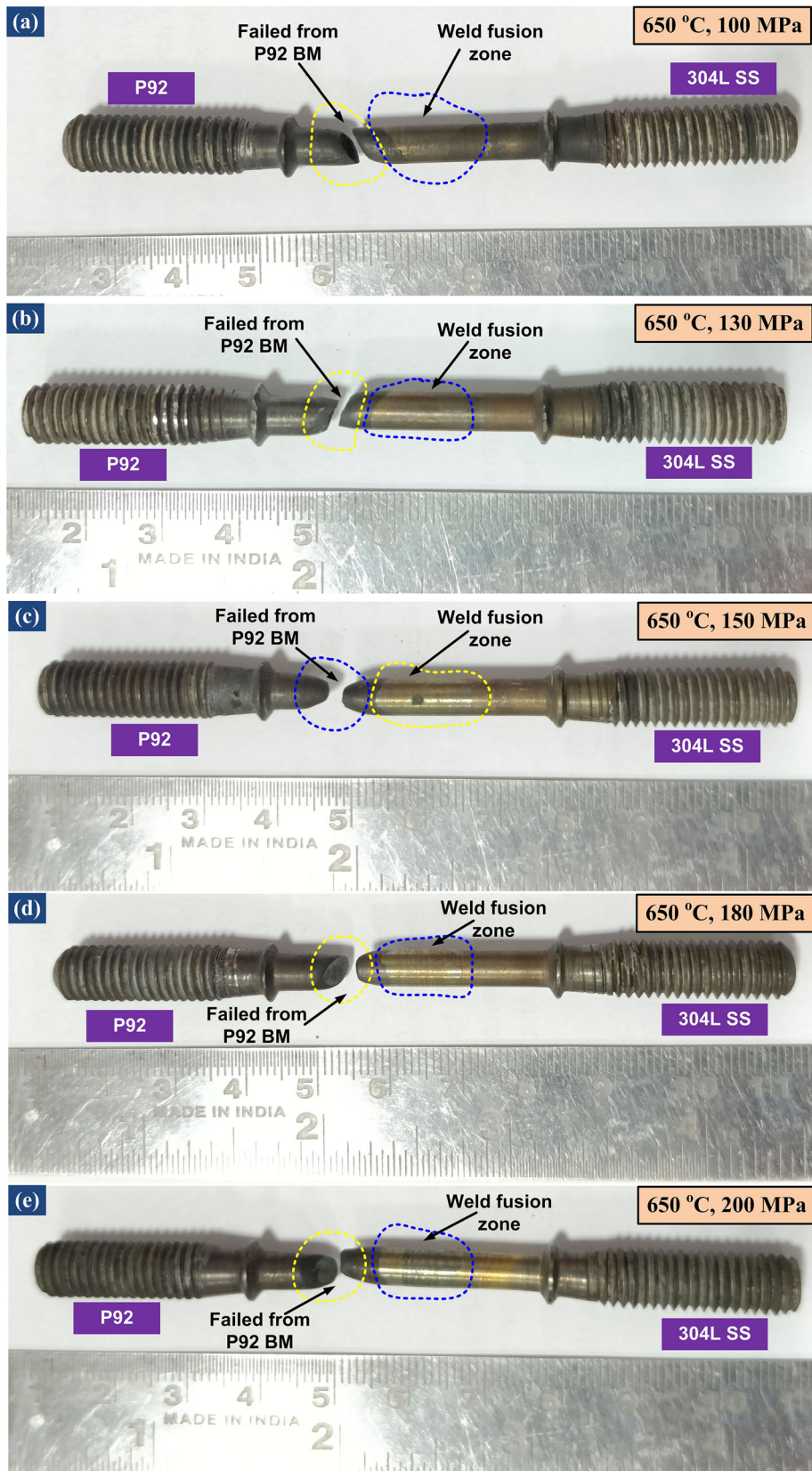
Fig. 11 P92/304L dissimilar weldments specimens tested at different creep tests condition: (a) 650 °C/100 MPa, (b) 650 °C/130 MPa, (c) 650 °C/150 MPa, (d) 650 °C/180 MPa, and (e) 650 °C/200 MPa
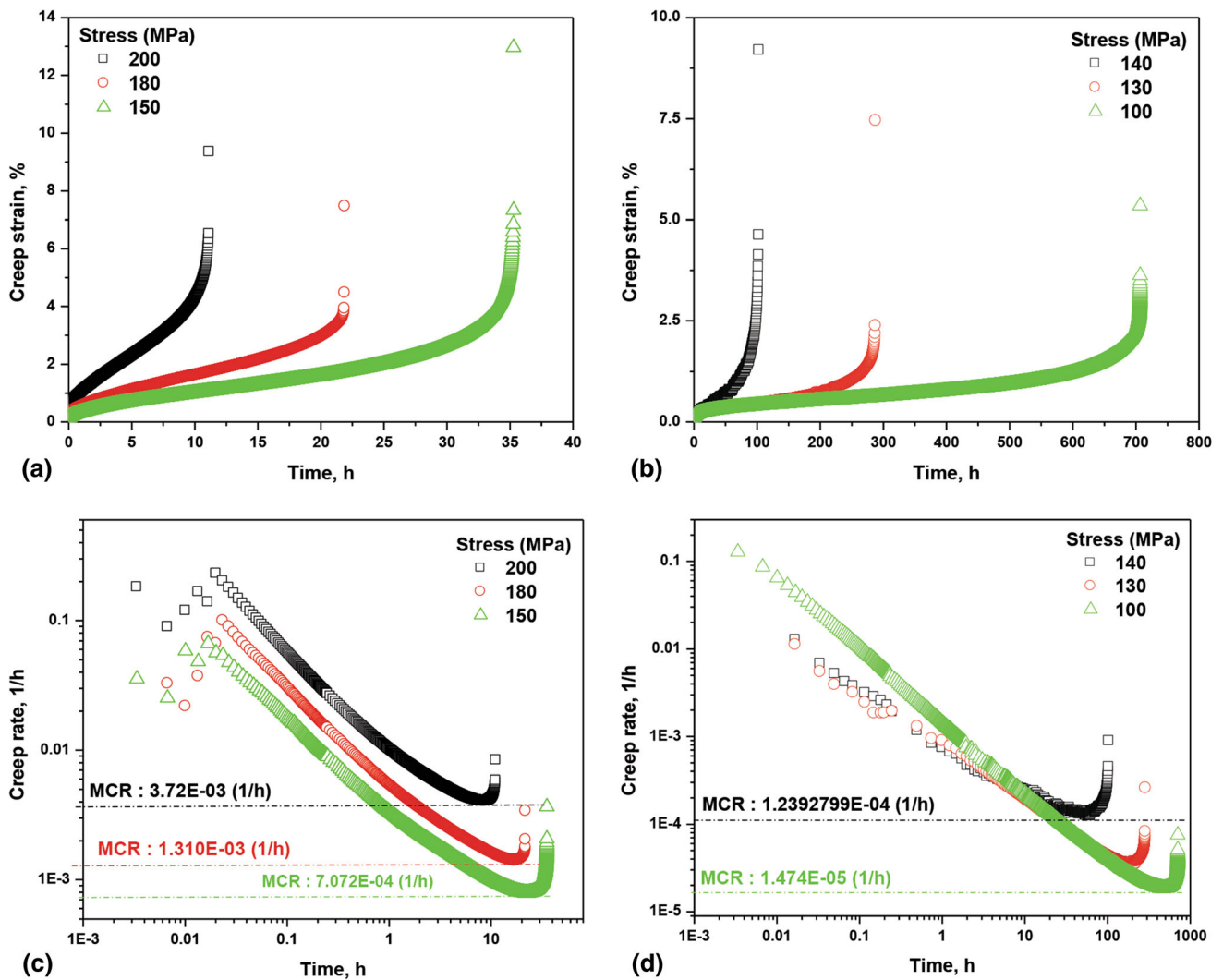
Fig. 12 Plot of creep strain as a function of time for P92/304L weld joints has been conducted at 650 °C under the stress range of 150-200 MPa and 100-140 MPa, as shown in (a) and (b), respectively. The corresponding creep rate vs. time plot is drawn in (c) and (d) to distinguish minimum creep rate (MCR) with respect to the applied stress

test temperature. The different stage of the creep curve, including the primary (transient), secondary (steady-state), and tertiary stage, was obtained for each test condition, as shown in Fig. 12(c), (d). Before the primary stage begins, there is instantaneous deformation due to the applied load on the specimen, which is insignificant. In the primary stage, the creep/strain rate decreases with time due to the work-hardening effect. Work hardening occurs due to the obstacles provided by the precipitates, sub-grains, free dislocations, and solid solution hardening. In this stage, the material gets hardened due to the restriction in the dislocation movement. In the second stage, the creep rate remains constant over time, mainly due to the balance between the work hardening and softening behavior of the material. Work hardening and recovery are two opposite mechanisms. In the third stage, a process occurs quickly due to the necking or crack formation with effective cross-sectional area decreasing till specimen failure. All the creep test results are listed in Table 2.

The creep test is a time-consuming process. Hence, it is not feasible to carry out the creep test for the entire creep life of the material. A mathematical relationship must be developed between the applied stresses and ruptured life. In the present investigation, the relationship between the applied stress (σ) and rupture time (t_r) was determined by using the linear regression analysis. On the X-axis, the independent variable (stress in the present case) and the dependent variable (rupture time) were chosen on the Y-axis. From the creep experimental data, it was pointed out that the rupture time varies quickly with the change in the applied stress (Table 2). Thus, log–log plot that has been plotted to obtain the best fit line of the data using linear fit analysis is shown in Fig. 13. The obtained R-squared value (coefficient of the determination) was close to 0.979, which indicates that the excellent fitting of the experimental data within the trend line. Wu et al. (Ref 41) also used a similar approach to develop the linear regression model between the applied stresses and rupture times. The obtained equation to predict the creep life at applied stress could be given by Eq 1:

$$\log(t_r) = \log(14.39695) + (-5.79039)\log(\sigma) \quad \text{(Eq 1)}$$

The other approach most frequently used to predict the creep life of the material is the Larson–Miller parameter equation. The creep life of the material depends upon the applied stress

Table 2 Creep test results of P92/304L weld joints (IN625 filler metal) at 650 °C under the various stress levels

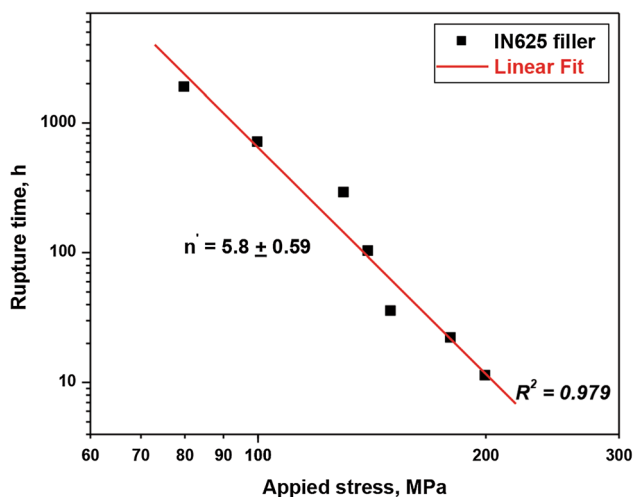| Temperature, °C	Stress, MPa	Creep strain, %	Rupture time, h	Elongation, %	Reduction area, %
650	100	5.35	706.9	5.35	43.11
650	130	16.94	288.3	7.45	42.31
650	140	18.02	103.5	18.02	72.17
650	150	12.97	35.3	12.97	68.06
650	180	7.46	21.9	7.46	47.12
650	200	9.35	11.2	9.35	48.11

Fig. 13 Plot of rupture time against the applied stress at 650 °C has been linearly fitted to find the stress exponent (n). The value of 'n' is found to be 5.8, and the creep mechanism falls under the dislocation climb-controlled process in the stress range of 80-200 MPa

Table 3 Rupture time and LMP values of P92/304L weld joints (IN625 filler metal) at 650 °C under various stress levels

Temperature, °C/K	Stress, MPa	Rupture time, h	LMP
650/923	100	706.9	21090
650/923	130	288.3	20730
650/923	140	103.5	20320
650/923	150	35.3	19889
650/923	180	21.9	19698
650/923	200	11.2	19428

and temperature. The LMP equation considers applied stress and temperature to predict the component's creep life. The LMP equation can be given by Eq 2 as follows (Ref 42):

$$LMP = T(C + \log t_r) \qquad (Eq\ 2)$$

where LMP is the Larson–Miller parameter, C is the Larson–Miller constant, t_r (h) is the rupture time, and T (K) is the test temperature. The value of C depends on the material; generally, it is in the range of 20-30 (Ref 43, 44). In the present case, the value of C is chosen 20 (Ref 45). Based on the reported data in Table 3, the plot of applied stress v/s LMP has been applied to
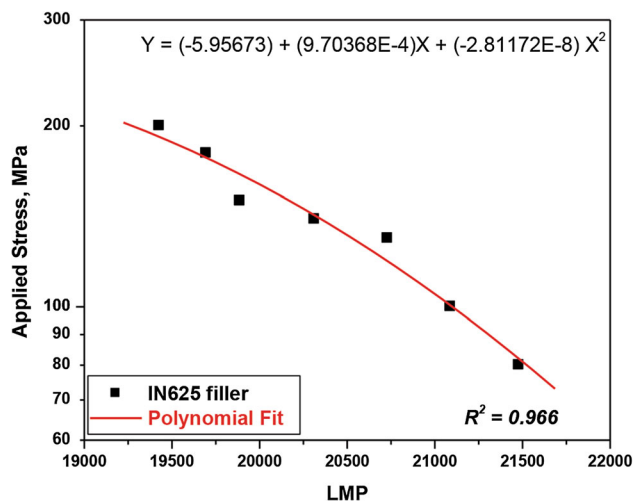

Fig. 14 Plot of applied stress against LMP at 650 °C has been fitted by applying the second-order polynomial fit in the stress range of 80-200 MPa. The constant value of LMP was taken as 20

the second-order polynomial fit, as shown in Fig. 14. From the trend line, the value of LMP can be obtained at a given applied stress. Therefore, the corresponding time to rupture can be calculated at 650 °C. Various researchers have also used this approach to predict the creep service life (Ref 46).

4.2 Macrostructure of the Fractured Creep Specimens

The creep behavior of the P92/304L dissimilar weld joint was investigated at 650 °C under the stress range of 100-200 MPa. The creep test specimen failed from the P92 steel parent metal side for all the test conditions. The creep fracture location depends upon the test condition, the parent metal used, and the welding process (Ref 24). The different creep service life was obtained for the specimen tested at different stress. The macrograph of the cross section of the fractured creep specimen is shown in Fig. 15(a)-(e). The macrograph consists of a fracture surface, parent metal, and weld metal. The flat fracture surface indicates the brittle fracture of the dissimilar weld joint. As shown in the macrograph of the fracture tip surface, the notch tip radius of the specimen tested is very less, indicating the plastic/brittle fracture of the creep specimen. The edges of the fractured surface inclined at 45° indicate the shear mode of the fracture. Thus, the creep specimen failed in the combined normal faulting and shear mode of the fracture. The macrographs of the cross section of the fractured creep specimen also confirm the excellent creep strength of the nickel-based filler metal and 304L austenitic stainless steel.
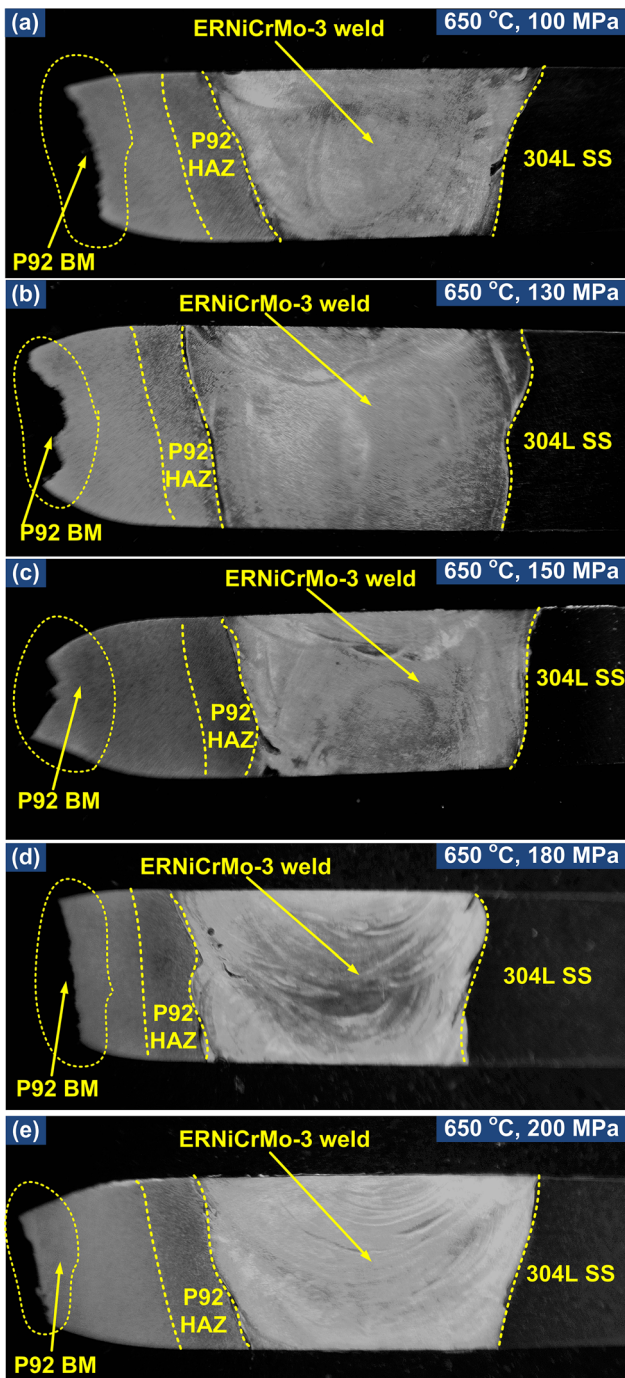
Fig. 15 Cross-sectional image of the creep ruptured specimen tested at 650 °C under the applied stresses of (a) 100 MPa, (b) 130 MPa, (c) 150 MPa, (d) 180 MPa, and (e) 200 MPa

4.3 Microstructure Changes After the Creep Test

The microstructure evolution near the fracture tip surface after the creep test is shown in Fig. 16(a)-(f) and 17(a)-(i). The large number of voids formed near the fracture tip surface indicates the extensive plastic deformation at the necking region. Comparatively higher numbers of the micro- and macro-voids were observed in the necking region compared to the CGHAZ and FGHAZ regions, as seen from the optical microscope image. The creep test at 650 °C with the applied stress range of 100-200 MPa showed no significant microstruc-

ture changes on the 304L side. The IN625 weld fusion zone also showed good stability during the creep test at 650 °C with an applied stress range of 100-200 MPa. The creep fracture was observed from the P92 steel parent metal side. The microstructural instability of the P92 steel at elevated temperature is the main limiting factor for its long-term service. The strength of the P92 steel is due to its tempered martensite lath structure with large numbers of dislocations. The dislocations are introduced into the metal during its manufacturing process (rolling process). The dislocations present in the metal help in plastic deformation. The movement of the dislocations causes the plastic deformation of the metal. However, if dislocations cannot move, plastic deformation does not occur. Solid solution strengthening and precipitation strengthening are the two basic mechanisms by which the motion of the dislocations is hindered. The movement of the dislocations is restricted by the precipitates present in the metal. Also, the movement of the dislocations is hindered at the grain boundaries due to the presence of the precipitates. $M_{23}C_6$ and MX precipitates are important for the creep strength of the P92 steel. The $M_{23}C_6$ precipitates are decorated along the grain boundaries. These precipitates maintain the creep strength of P92 steel by hindering the motion of the dislocations and grain boundaries. However, the combined strengthening effect by the above discussed mechanism may change at elevated temperature service. The coarsening of the $M_{23}C_6$ precipitates during the high-temperature service influences the creep strength of the steel. The finer precipitates effectively pin the boundaries and dislocations compared to the coarse precipitates (Ref 21). The formation of the creep cavity starts along the prior austenite grain boundaries. It is because grain boundaries become weak at high temperature due to the precipitate coarsening and loss of the solid solution strengthening elements. Also, the formation of the laves phase [Fe_2 (Mo, W)] after long-term exposure provides precipitation strengthening. However, this effect lowers after the coarsening of the laves phase (Ref 47). The laves phase provides the possible nucleation sites for the creep cavities. The high-stress concentration at this place converts the cavities into micro-cracks. These micro-cracks later transformed into macro-cracks and caused the fracture from the P92 steel (Ref 47). The formation of the laves phase also results in the loss of the solid solution strengthening W and Mo elements from the P92 steel matrix. At low-stress condition, when the rupture time is high, the fracture from the P92 steel is due to the formation of the laves phase.

The FESEM microstructural investigation at the fracture tip surface, weld interface, and weld fusion zone was also carried out for the creep ruptured specimen. The FESEM image of the microstructure evolution toward the P92 steel side after the creep test at 650 °C under 100 MPa is shown in Fig. 18(a)-(f). The creep cavities formed near the fracture surface are shown in Fig. 18(b)-(c). The FESEM microstructure of the ERNiCrMo-3 weld fusion zone and parent metal interface is shown in Fig. 18(d)-(f). The grain boundary sliding and diffusion are the two main plastic deformation mechanisms during creep tests. During the creep service, a cavity is formed around the prior austenite grain boundaries due to the grain boundary sliding. The FESEM image of the microstructure evolution toward the P92 steel side after the creep test at 650 °C under 130 MPa is shown in Fig. 19(a)-(d). The microstructure of the P92 CGHAZ region with voids formed along the PAGBs after the creep test is shown in Fig. 19(d). From the FESEM microstructure, it can be seen that the precipitation of the $M_{23}C_6$ carbides increased
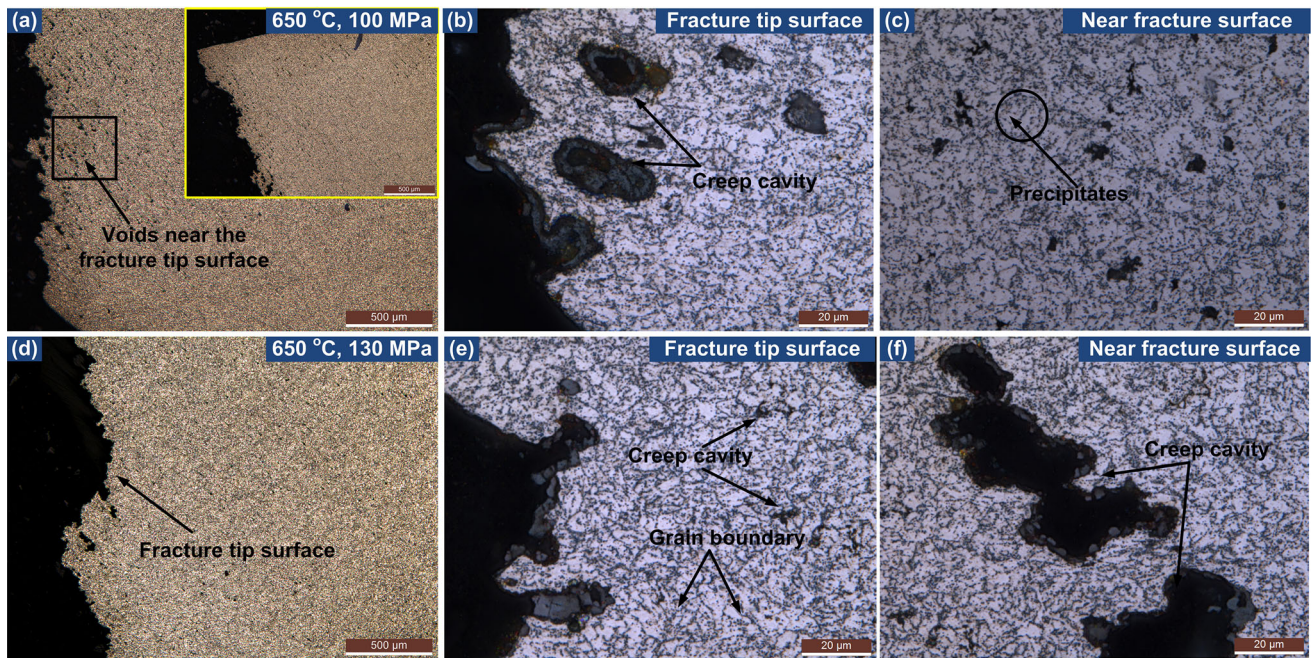
Fig. 16 (a) Optical microstructure of the creep rupture specimen tested at 650 °C/100 MPa: fracture surface, voids, and cavities can be observed, (b) microstructure of the fracture tip surface, (c) microstructure near the fracture surface, (d) microstructure of the creep rupture specimen tested at 650 °C/130 MPa: fracture surface, (e) microstructure of the fracture tip surface, and (f) microstructure near the fracture surface

significantly after the creep test. The undissolved precipitates tend to coarsen during the creep service. The creep strain causes the additional precipitation of the $M_{23}C_6$ carbides and the coarsening of the existing $M_{23}C_6$ precipitates. The coarsening of the $M_{23}C_6$ precipitates results in a decrease in the number density of the precipitates. This ultimately degrades the precipitation-strengthening mechanism. The formation of the laves phase and $M_{23}C_6$ phase takes place during the elevated temperature creep exposure. A significant amount of the W and Mo is consumed during the formation of this phase, which ultimately reduces the solid solution strengthening. During elevated temperature service, the $M_{23}C_6$ precipitates and laves phases grow rapidly along the PAGBs. The FESEM-EDS point and area map analysis were conducted near the fracture tip surface containing coarse and fine secondary phase particles around the cavity to identify the composition of the secondary phase. The EDS results showed a strong peak of the W elements. The dominating particles near the creep cavities are rich in Cr and W elements. Such particle was identified as the laves phase and carbide precipitates. The possible laves phase can be $(Fe, Cr)_2(W, Mo)$ type laves phase and $(Fe, Cr)_{23}C_6$ secondary precipitates (Ref 22). The FESEM-EDS area mapping analysis revealed the spot of the W element. Thus, the possible laves phase can be $(Fe, Cr)_2(W)$ type. Also, P92 steel (W:2 wt.% max., Mo:0.6 wt.% max.) has a higher amount of the W and less amount of the Mo element in its chemical composition compared to the P91 steel (W: nil, Mo:1.05 wt.% max.) (Ref 48). Thus, the majority of the laves phase formation is of $(Fe, Cr)_2(W)$ type instead of $(Fe, Cr)_2(Mo)$ type in the P92 steel. The $(Fe, Cr)_2(Mo)$ type laves phase mostly forms in P91 steel (Ref 49). The EDS elemental map of the creep cavity present near the fracture tip surface is shown in Fig. 20. The spot of the Cr and W elements was observed from the area map analysis. The chemical composition of the various particles

determined by EDS is listed in Table 4. The EDS line scan was performed at the parent metal and weld metal interface to identify the element distribution in gradient microstructure, as shown in Fig. 21(a)-(d). The steep variation of the Cr, Ni, and Fe elements was observed at the weld fusion line, which was in accordance with the chemical composition of the base and weld metal. The EDS line scan result showed no significant diffusion of the elements from the base to weld metal and vice versa after the creep test at a longer duration. The solidification of the weld pool after welding leads to the segregation of the various elements. This segregation causes the formation of the laves phase in the weld fusion zone. The EDS map of the secondary phase particle developed in the weld fusion zone due to the rapid cooling after welding is shown in Fig. 21(e). The segregation of the Nb, Mo, and Ti can be observed from the map. The segregation of Mo and Nb takes place in the inter-dendritic region due to their distribution coefficient value of less than 1. The depletion of the Fe and Cr elements can be observed from the area map. The composition of these particles determined by EDS point analysis is listed in Table 4. Based on the published results, the possible secondary phase formation can be $(Nb, Ti)C$ (Ref 50). As the specimen was fractured from the P92 steel side for all the creep test condition, the major aim of this study was to perform a detailed microstructural investigation of the P92 side. The FESEM microstructure evolution toward the P92 steel side after the creep test at 650 °C under the stress range of 150-200 MPa is shown in Fig. 22(a)-(i). The formation of the laves phase was not observed for this test condition. The coarse carbide precipitates were only observed around the cavity.

There are different factors/mechanisms that influence the creep deformation of the material. The performance of the P92 steel at elevated temperature service depends upon its ability to resist the dislocation movement. The glide (motion of disloca-
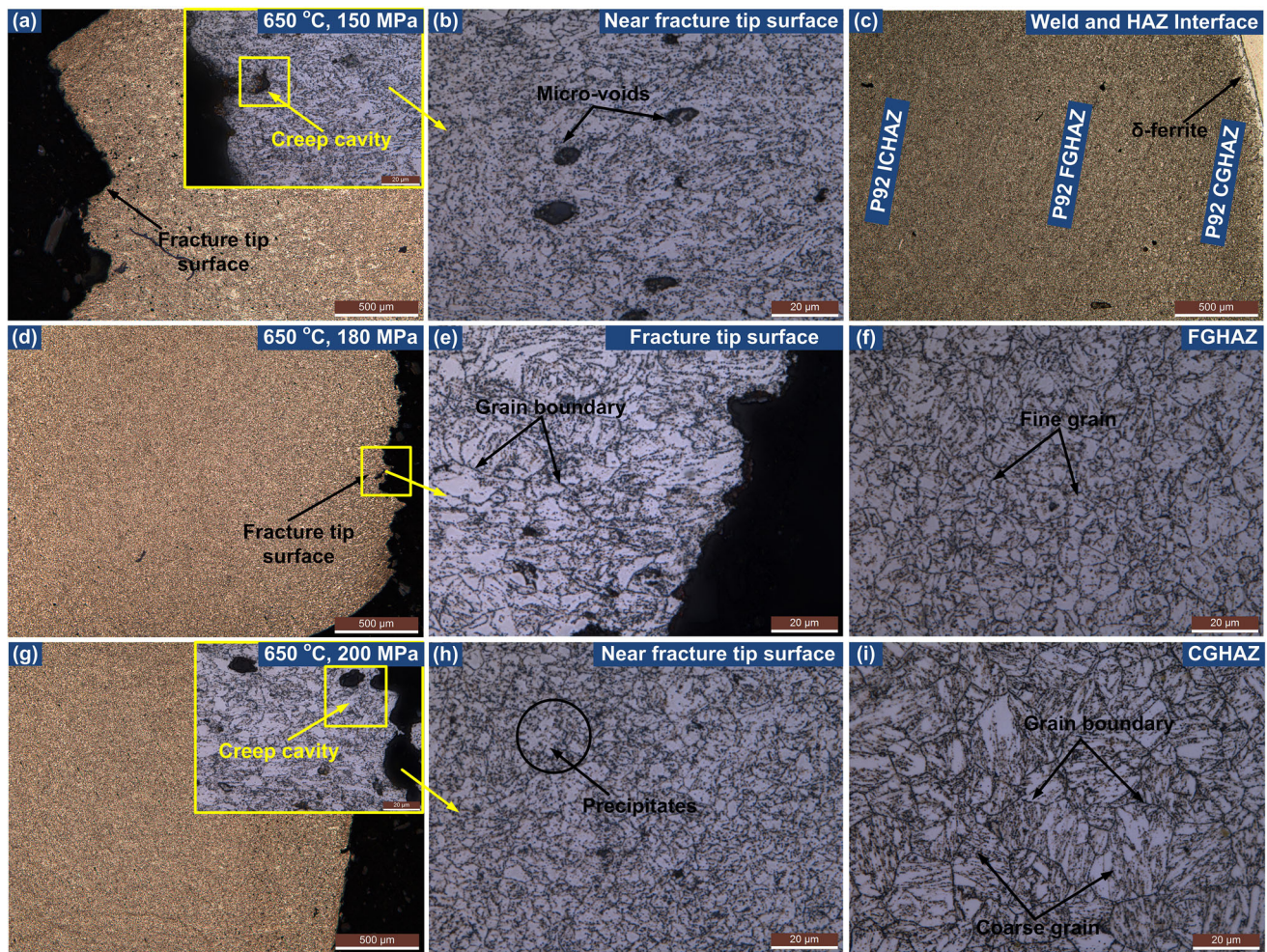
Fig. 17 (a) Optical microstructure of the creep rupture specimen tested at 650 °C/150 MPa: fracture surface (b) microstructure near the fracture tip surface (c) microstructure at the weld and P92 HAZ interface, (d) microstructure of the creep rupture specimen tested at 650 °C/180 MPa: fracture surface, voids, and cavities can be observed (e) microstructure of the fracture tip surface, (f) microstructure at the P92 FGHAZ region, (g) microstructure of the creep rupture specimen tested at 650 °C/200 MPa: fracture surface, voids, and cavities can be observed, (h) microstructure near the fracture tip surface, and (i) microstructure at the P92 CGHAZ region

tion in its slip plane) and climb (motion of dislocation in adjacent parallel slip plane) of the dislocation in the lattice cause creep. The $M_{23}C_6$ carbides and MX carbonitrides precipitates retard the movement of the dislocations. Also, the number density of the $M_{23}C_6$ carbide precipitates in the parent metal matrix is higher compared to the MX precipitates due to the increased weight percentage of the Cr element in the alloy composition. Thus, the stability of the $M_{23}C_6$ carbides is more critical to maintain the creep strength of the P92 steel at elevated temperature service. The absence of a pinning effect by these precipitates is mainly responsible for the void formations along the grain boundaries due to the lack of boundary strengthening. The MX carbonitride precipitates have a small size and low coarsening rate at elevated temperature service. These precipitates provide stable precipitation hardening to the P92 steel. However, $M_{23}C_6$ carbide precipitates have a big size and high coarsening rate at elevated temperature service. Due to this, the pinning effect of these particles on lath boundaries disappears once these precipitates coarsen. Also, the dissolution of the $M_{23}C_6$ carbides during the welding leads to the high concentration of the C and Cr elements in the matrix. During creep, the C and Cr elements re-precipitate on the

remaining particles, resulting in coarse precipitates. This phenomenon mainly causes the tri-axial stress concentration between the coarse precipitates and the base metal matrix. This ultimately leads to the softening of this region and void generation near the coarse precipitates (Ref 18). After the creep test, the microstructure near the weld interface, CGHAZ, and FGHAZ region was similar to the microstructure after post-weld heat treatment. Very few voids can be observed near the weld interface, CGHAZ, and FGHAZ region. After the creep test, the lath structure was observed in the CGHAZ and FGHAZ regions. The CGHAZ and FGHAZ regions showed the prior austenite grain structure with grain boundaries.

The schematic diagram of the failure mechanism from the martensitic steel after elevated temperature and stress condition is shown in Fig. 23. The microstructure of the P92 steel is composed of tempered martensite lath structure, $M_{23}C_6$ carbide, and MX carbonitride precipitates, as discussed in the introduction section. The formation of the new $M_{23}C_6$ precipitates and the coarsening of the existing $M_{23}C_6$ precipitates increases with the increase in the creep strain. The grain boundaries mainly provide strengthening against creep failure. The $M_{23}C_6$ carbide precipitates mainly consist of Cr (M stands
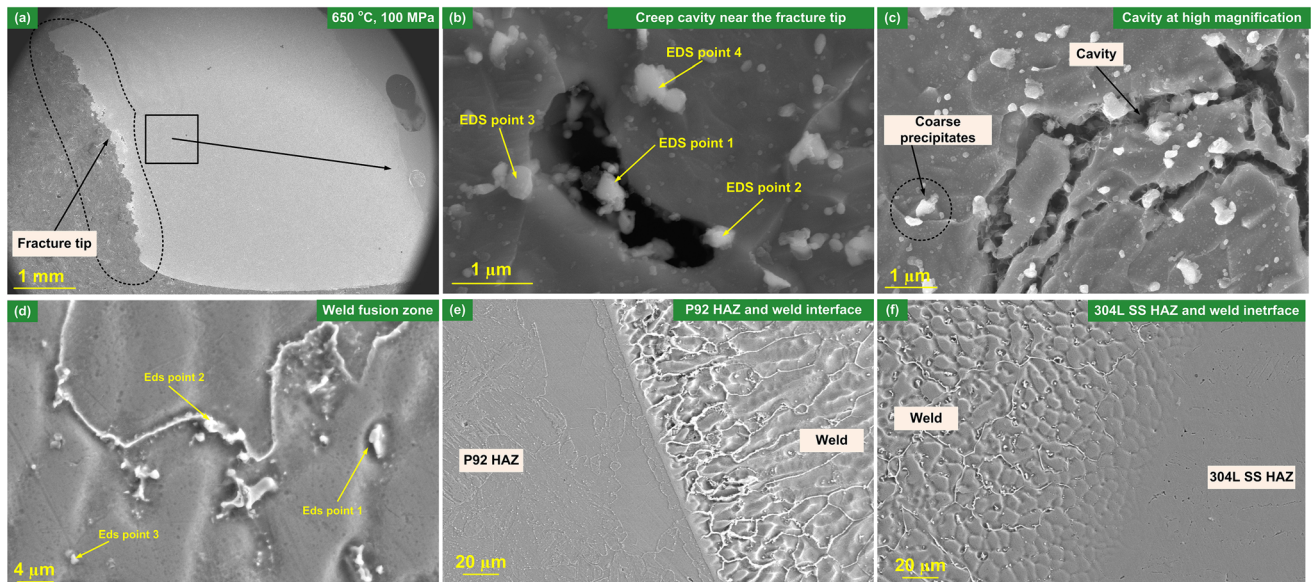
Fig. 18 (a) FESEM microstructure of the creep rupture specimen at 650 °C/100 MPa: fracture tip surface, (b-c) creep cavity near the fracture tip surface at high magnification, (d) microstructure of the ERNiCrMo-3 weld fusion zone, (e) P92 HAZ and weld interface, and (f) 304L HAZ and weld interface
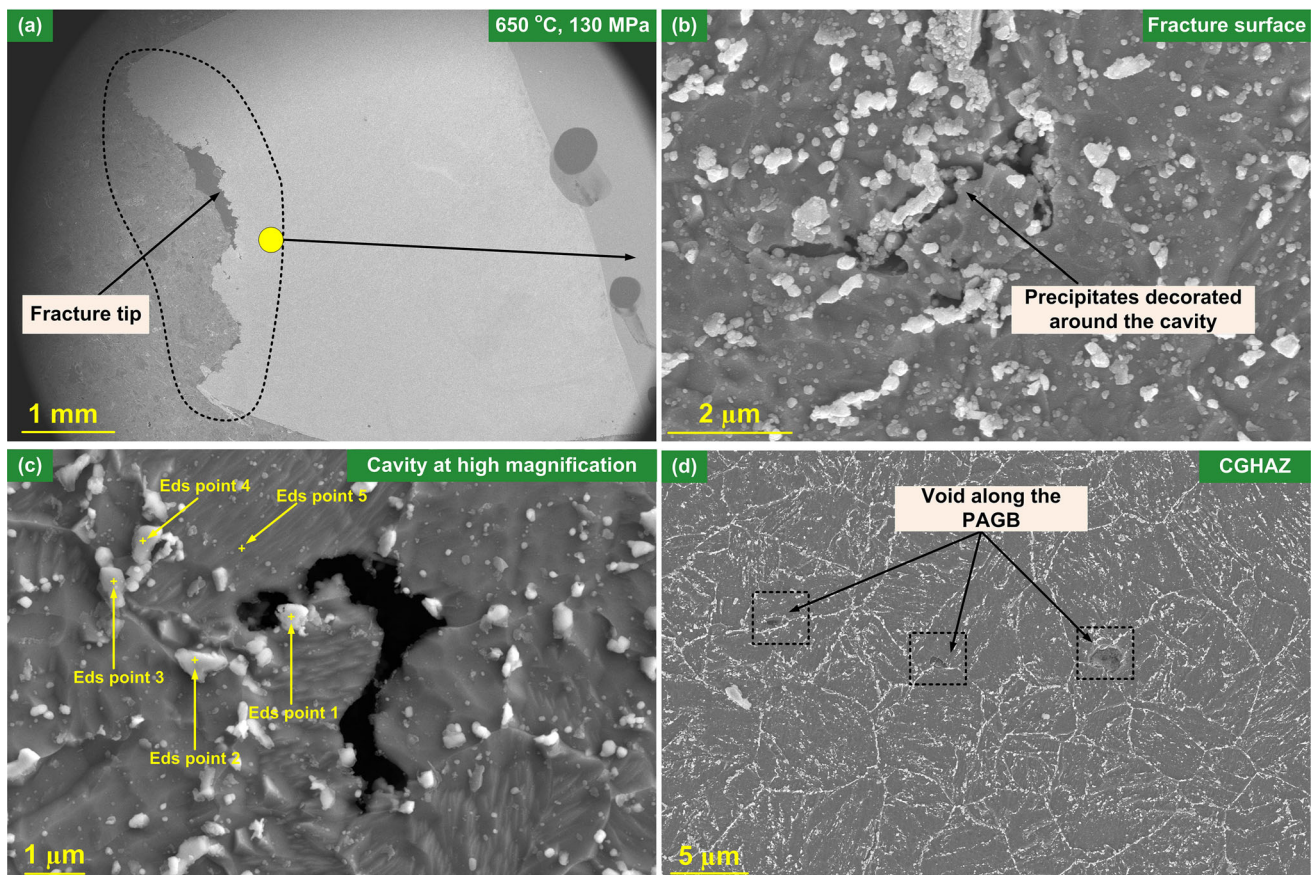

Fig. 19 (a) FESEM microstructure of the creep rupture specimen at 650 °C/130 MPa: fracture tip surface, (b) microstructure near the fracture tip surface, voids can be seen, (c) creep cavity near the fracture tip surface at high magnification, and (d) microstructure of the CGHAZ region, voids can be seen along the PAGBs
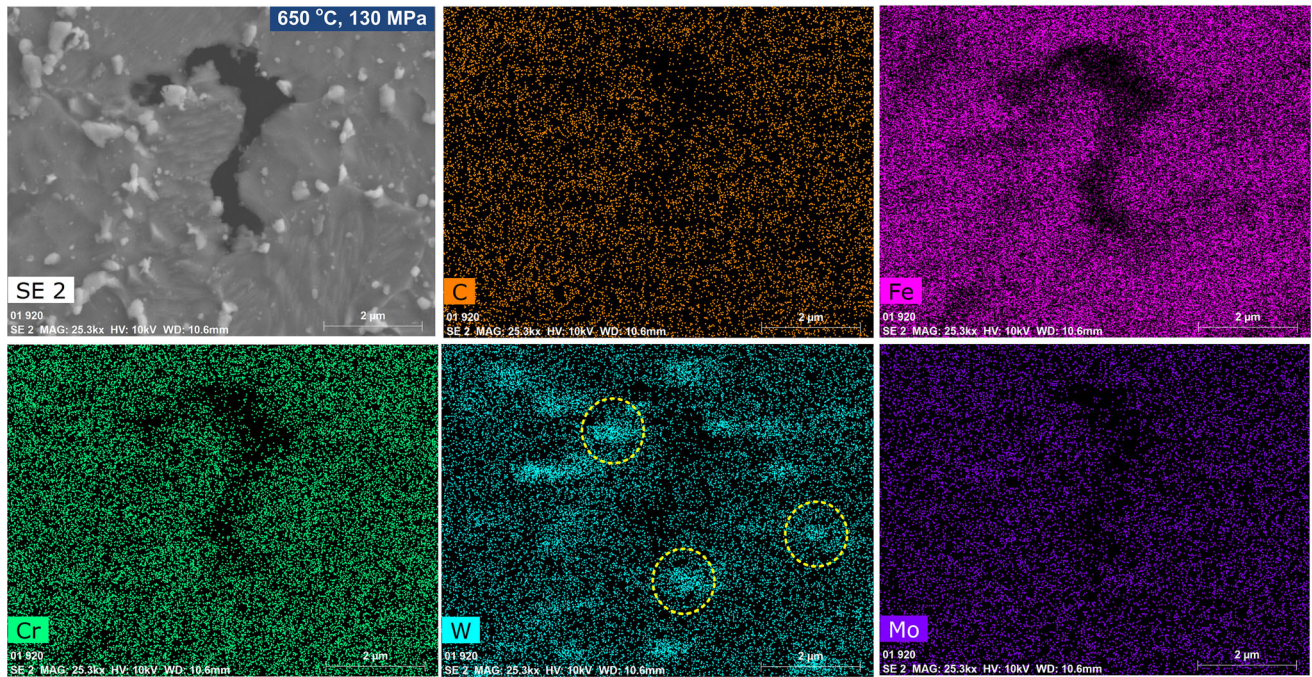
Fig. 20 EDS elemental map of creep cavity present near the fracture tip surface for the specimen tested at 650 °C, 130 MPa, Fig. 19(c) (few W element spots are marked by a circle)

Table 4 EDS results of the different particles near the fracture surface

	Location	C	Fe	Cr	Mo	Nb	Ni	W	Ti
Fig. 18(b)	1	22.97	62.61	6.55	0.0	1.91	0.29	5.63	…
	2	19.17	69.87	6.23	0.0	1.63	0.24	2.36	…
	3	17.92	65.28	6.05	0.02	1.82	0.10	5.37	…
	4	15.19	72.53	7.14	0.0	1.51	0.20	2.22	…
Fig. 19(c)	1	9.12	60.39	8.50	1.28	4.48	1.07	15.88	…
	2	17.61	57.51	5.74	…	2.54	0.59	4.27	…
	3	15.22	41.57	20.88	0.27	3.75	0.45	8.58	…
	4	22.06	40.50	15.06	…	4.04	0.79	2.66	…
Fig. 18(d)	1	6.5	27.6	18.2	4.7	2.4	40.5	…	0.2
	2	11.9	17.7	14.3	11.7	13.2	30.9	…	0.2
	3	23.8	15.6	11.4	8.7	16.5	22.7	…	1.2

for Cr) and C in their composition. The dissolved Cr and C re-precipitate during the high-temperature working environment. This results in the coarsening of the $M_{23}C_6$ carbide precipitates. The formation of the laves phase starts after 100 h of service at the elevated temperature of 650 °C. The mechanism of the laves phase formation is as follows. The laves phase develops near the chromium-depleted region adjacent to the $M_{23}C_6$ carbide. Thus, before the formation of the laves phase, the formation of the $M_{23}C_6$ carbide is required. The region adjacent to the $M_{23}C_6$ carbide has a high concentration of the W and Mo elements, which act as a possible site for the laves phase formation (Ref 22). The laves phase forms at the prior austenite grain boundaries at the cost of consumption of the important solid solution strengthening W and Mo elements from the base metal matrix. Thus, the solid solution strengthening provided by the W and Mo elements weakened. The formation of the laves phase results in the softening of the parent metal matrix, providing a possible nucleation of the creep cavities. Thus, a micro-void is created around these coarse secondary phase

particles during the applied tension load. These micro-voids later converge together and form the crack. Thus, failure of the DWJs takes place before the actual service life. When the applied stress is high, the laves phase does not form due to the low service time. In this condition, failure occurs due to the plastic deformation caused by the grain boundary sliding in the base metal. This large plastic deformation forms dimples of various shapes and sizes along the prior austenite grain boundaries (PAGBs), resulting in the transgranular fracture (Ref 51).

4.4 Micro-hardness Distribution After Creep Test

The micro-hardness across the different zones of the fractured specimen was measured, i.e., fracture region, HAZ, parent metal, and weld metal. The Vickers micro-hardness distribution over the cross section of the creep tested specimen is shown in Fig. 24(a)-(e). The micro-hardness investigation can be helpful in determining the approximate location of the
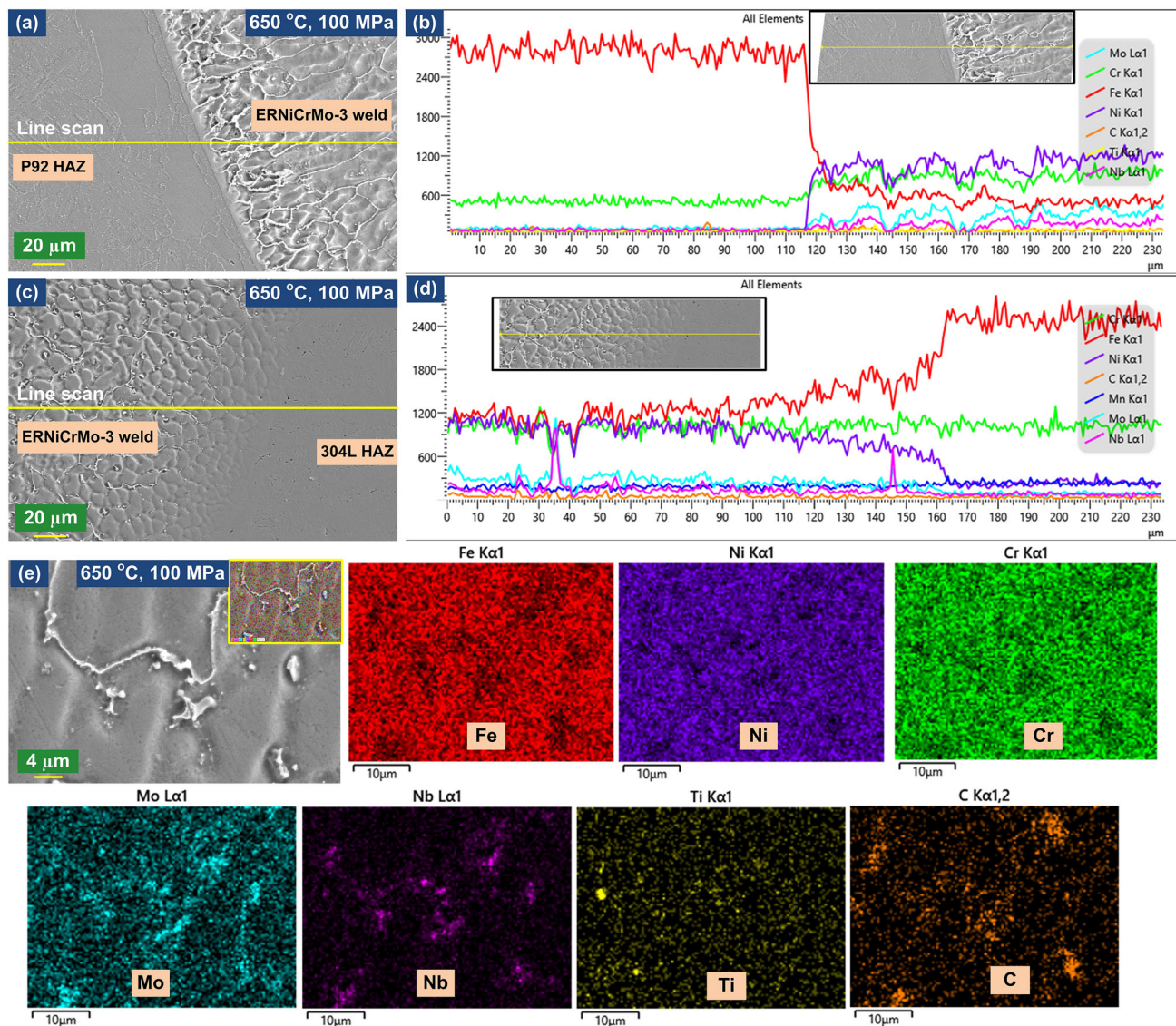
Fig. 21 For the specimen creep tested at 650 °C, 100 MPa (a-b) EDS line scan results across P92 HAZ and ERNiCrMo-3 weld interface, (c-d) EDS line scan results across 304L HAZ and ERNiCrMo-3 weld interface and (e) EDS elemental map of ERNiCrMo-3 weld metal

fracture of the material during the elevated stress and temperature service. With the fracture tip surface set as a reference point (X = 0), the hardness measurement was performed across the P92-ERNiCrMo-3-304L dissimilar weld joint. Each location has a different micro-hardness value depending upon its microstructural characteristics. The fracture location was observed in the P92 steel parent metal for all the test condition. The failure occurred from the P92 steel due to the softening of the parent metal matrix. The hardness was measured at the fracture region and found to be decreased with the lowest value ($\sim$ 173 HV) compared to the hardness of the as-received P92 steel ($\sim$ 235HV). Thus, the hardness of the P92 steel was decreased after the creep test. The minimum hardness value was observed near the fracture tip surface due to the softening mechanism occurring at the breaking point because of the extensive plastic deformation. The coarsening of the $M_{23}C_6$ precipitates is mainly responsible for the drop in the hardness near the fracture tip surface, as well as in the loss of the carbon and alloying elements, which are responsible for the precipitation strengthening of the P92 steel. The micro-hardness value

is affected by the microstructural evolution during the creep exposure. The drop in the hardness value was due to the loss of the solid solution strengthening and precipitation strengthening due to the coarsening of the precipitates and formation of the laves phases. Also, the hardness value significantly drops at the location of the large numbers of voids present across the fracture surface. As the distance from the fracture point increases, the hardness gradually increases. After welding, the maximum hardness was observed in the CGHAZ and FGHAZ regions. After the creep test, the hardness of the CGHAZ and FGHAZ regions was decreased due to the tempering effect. The hardness value decreases with the increase in the creep service time. The ICHAZ region has minimum micro-hardness value among the P92 HAZ region after the creep test at different conditions. After welding, 304L parent metal has a hardness value of $\sim$ 185HV. After the creep test, the hardness of the 304L parent metal barely changed as the obtained hardness value was similar to the value obtained after the welding. After welding, ERNiCrMo-3 weld metal has a hardness value of $\sim$ 195HV. After the creep test, the hardness of the
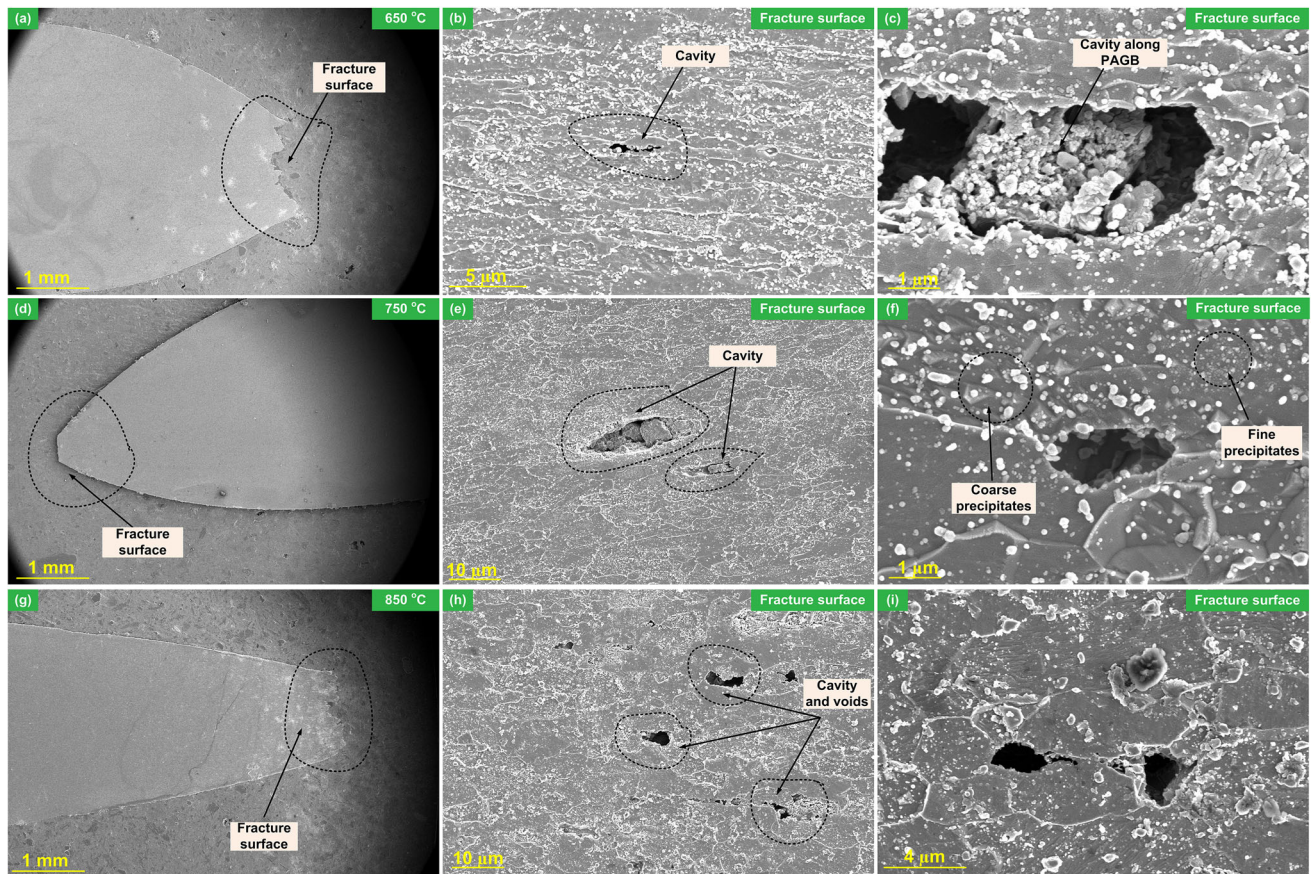
Fig. 22 (a) FESEM microstructure of the creep rupture specimen at 650 °C/150 MPa: fracture surface, (b) microstructure of the fracture surface, voids can be seen, (c) microstructure of the CGHAZ region; voids can be seen along the PAGBs, (d) FESEM microstructure image of the creep rupture specimen tested 650 °C/180 MPa: fracture surface, (e) microstructure of the fracture surface, voids can be seen, (f) microstructure of the FGHAZ region, (g) FESEM microstructure of the creep rupture specimen tested at 650 °C/200 MPa: fracture surface, (h) microstructure of the fracture surface, voids can be seen, and (i) microstructure of the CGHAZ region, void can be seen
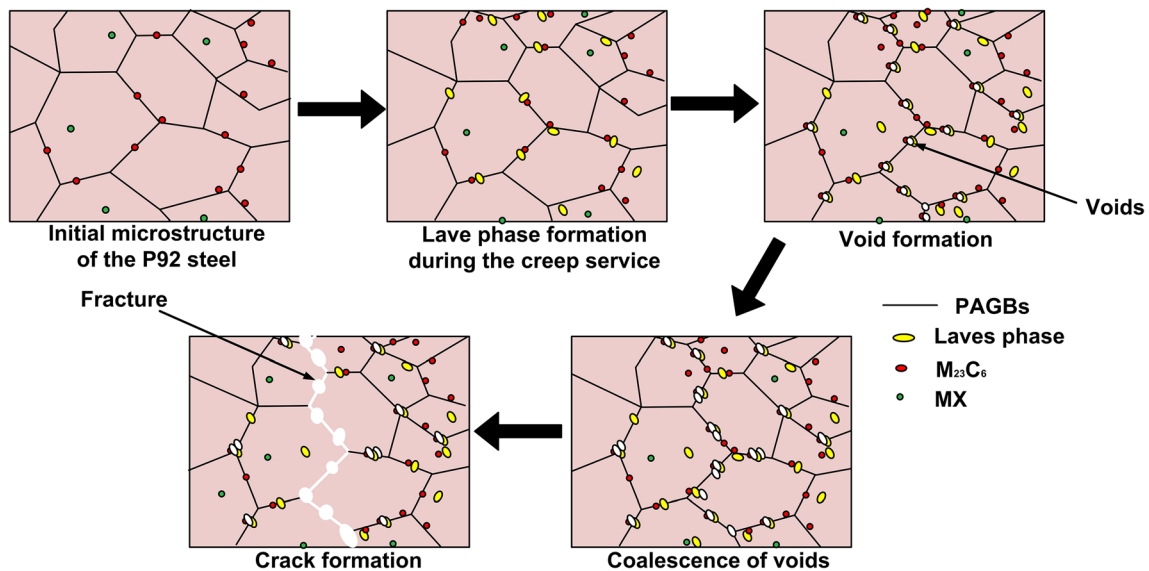

Fig. 23 Failure mechanism of the P92 steel [41]. Reprinted from Engineering Failure Analysis, Vol 125, Guanzhi Wu, Kai Ding, Tao Wei, Shangfei Qiao, XiaLiu, Yulai Gao, Rupture behavior and fracture mode for Inconel625-9% Cr steel dissimilar welded joints at high temperature, Article No. 105412, Copyright 2021, with permission from Elsevier
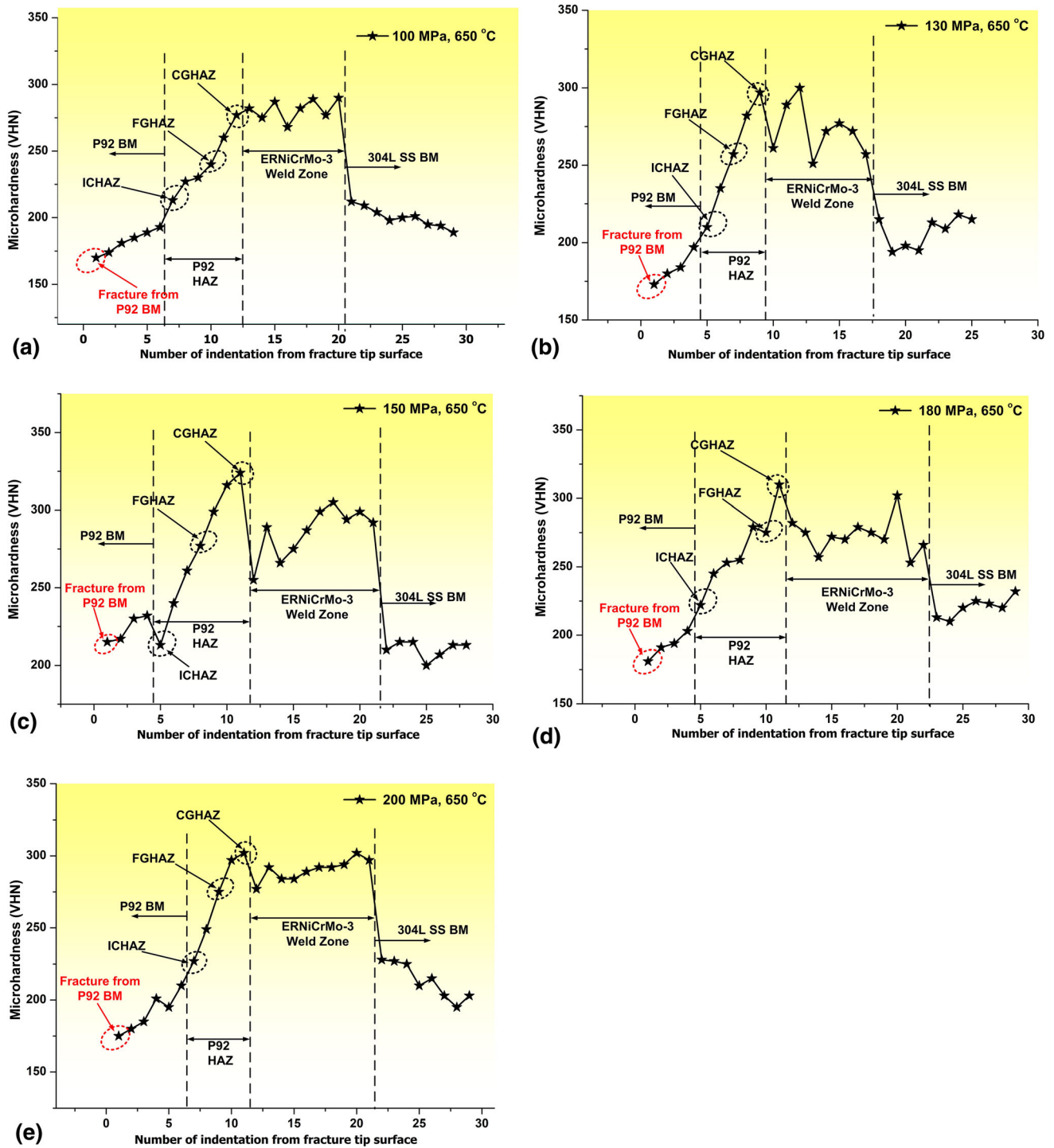
Fig. 24 Micro-hardness profile across the cross section of the fractured creep specimens

ERNiCrMo-3 weld metal increased due to the precipitation hardening effect.

4.5 Fracture Surface Analysis of Creep Specimen

The SEM microstructure of the fractured creep specimen at low magnification is shown in Fig. 25(a)-(e). A low-magnification image shows the overall appearance of the fracture surface containing voids, cracks, and sheared edges. The SEM microstructure at higher magnification is also shown in subsequent images (figures adjacent to the low-magnification image). The fractured surface showed that the plastic deformation occurred in normal mode at the center region of the surface and in shear mode at the edge of the surface. This shows the combined mode of the fracture at elevated temperature. The typical cup and cone fracture mode was completely absent for the creep specimen. The fracture surface microstructure of the specimen tested at 100 and 130 MPa exhibited the secondary phase particles inside the voids. The EDS result of the secondary phase particle was as follows: C: 26.65%, Cr:
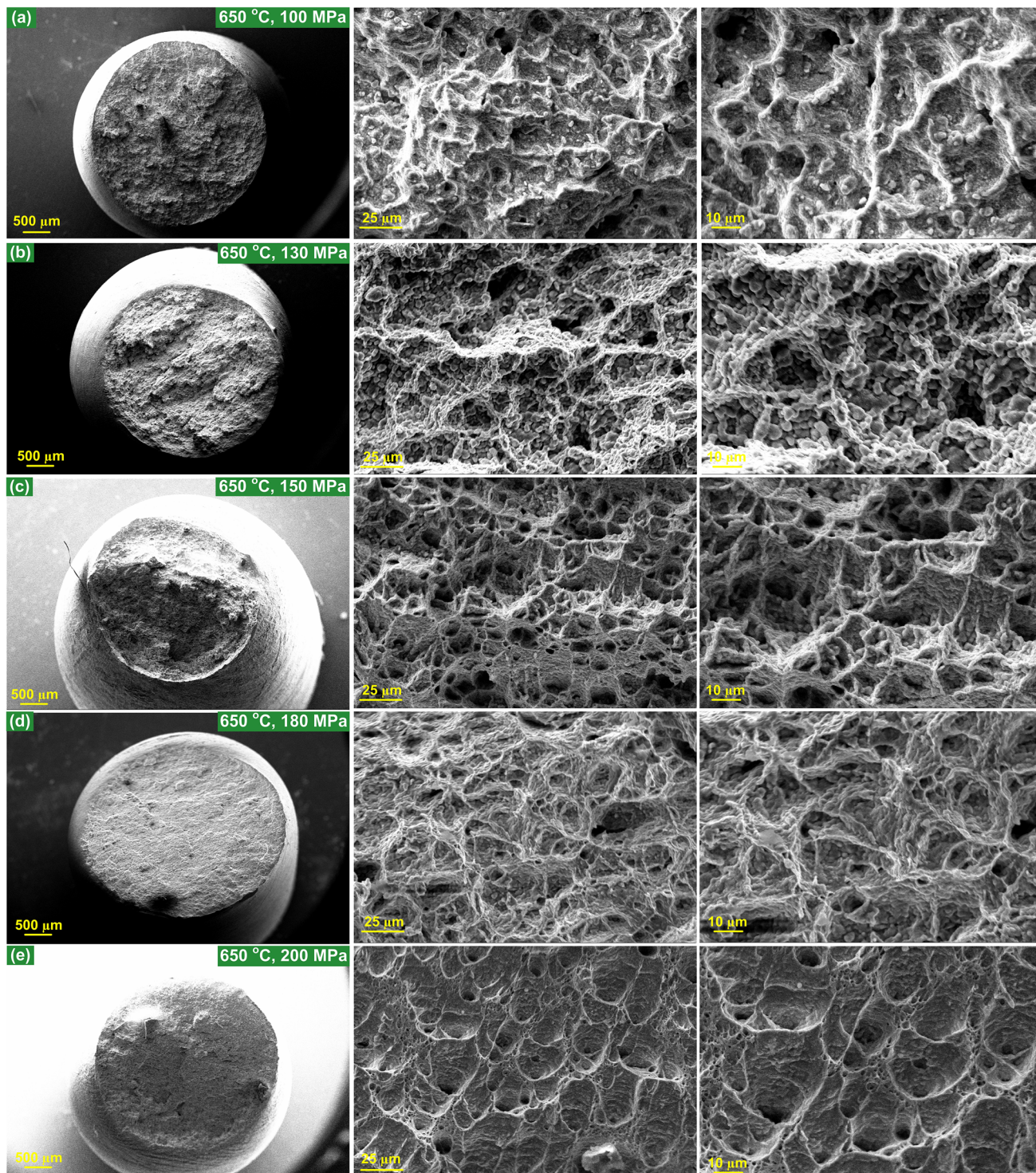
Fig. 25 SEM microstructure of the fracture surface of the creep ruptured specimens shown at low and high magnification, which was tested at 650 °C under various applied stresses of (a) 100 MPa, (b) 130 MPa, (c) 150 MPa, (d) 180 MPa, and (e) 200 MPa

7.11%, Fe: 63.99%, W: 2.06%, Ti: 0.04%, Mo: 0.15%. The particles were rich in Fe and Cr, indicating the $M_{23}C_6$-type carbide particles at the fracture surface. The fracture surface of the specimen tested at 150 MPa exhibits large numbers of micro-voids, big cavities, and coarse dimples, indicating the ductile mode of the failure with slight shearing at the edges of the fracture surface. The flat fracture surface appearance was observed from the low-magnification image for the specimen tested at 180 and 200 MPa. The fracture surface is composed of large numbers of the cleavage planes separated by the tearing ridges. Very few voids and incomplete parabolic dimples were observed on the fracture surface. Also, no significant necking was observed for the fractured creep specimen, indicating a ductile–brittle fracture mode at 180 and 200 MPa.

5. Conclusions

In this study, the creep and high-temperature tensile performance of the P92/304L dissimilar weld joint under different stress and temperature condition was investigated. Based on the results, the main findings from this study are as follows:

(1) It was found that the dissimilar weld joint failed from the 304L steel parent metal region during the elevated temperature tensile tests at 450 and 550 °C. The failure from the 304L steel parent metal region during the test at 450 and 550 °C was easily identifiable, as HAZ formation was insignificant toward the 304L side. Also, the jerky flow behavior of the stress–strain curve was observed at 450 and 550 °C test temperature due to the DSA phenomenon occurring in the 304L steel.

(2) As the tensile test temperature increased from 550 to 650 °C, failure occurred from the P92 steel parent metal region. The analyzed tensile test data at 650, 750, and 850 °C indicated the quick degradation of the microstructural and mechanical properties of the P92 steel with an increase in temperature. The absence of the lath martensite structure and void formation along the PAGBs due to the precipitates coarsening at 650-850 °C temperature range induce the failure from the P92 steel. This microstructural evolution leads to the depreciation of the mechanical properties. The UTS and YS value falls rapidly with the rise of the test temperature. The UTS value decreased from 439 to 58 MPa, and YS fell from 155 to 41 MPa during the test from 450 to 850 °C.

(3) SEM fractography analysis of the ruptured surface of the high-temperature tensile specimen showed the ductile–brittle mode of the failure for the specimen failed from the 304L steel. The brittle mode of the failure occurred due to the low ductility and high hardness of the 304L steel at 450-550 °C test temperature. However, completely ductile mode of the fracture was observed for the specimen that failed from the P92 steel. The large number of small dimples on the fracture surface of the P92 steel indicated the good plasticity of the P92 steel in the temperature range of 650-850 °C.

(4) Micro-hardness examination after the high-temperature tensile test showed the increase in the hardness value of the 304L steel at fracture tip surface (~320HV) compared to the 304L parent metal (~190HV). The increase in the hardness is due to the strain hardening phenomenon.

(5) From the creep test conducted at 650 °C in the stress range of 100-200 MPa, it was found that the fracture was always from the P92 steel parent metal side, irrespective of the test condition. Under low-stress condition, laves phase formation due to the consumption of the W and Cr elements leads to the fracture from the P92 steel. Under high-stress condition, the extensive plastic deformation caused by the grain boundary sliding leads to the failure.

(6) The minimum micro-hardness value was observed at the necking region for specimens that failed from the P92 steel during the creep. The hardness drop near the fracture tip surface and region of extensive cavity formation indicates the strength reduction due to the loss of the precipitation and solid solution strengthening effect. It was observed that the P92 HAZ region, IN625 weld fusion zone, and 304L were free from the fracture during the creep and were less affected by high-temperature exposure, which can also be correlated with the micro-hardness value in these regions.

(7) SEM fractography was also performed to ascertain the fracture mode and microstructure of the fracture surface at various creep test condition. The obtained fractograph at 650 °C in the stress range of 100-130 MPa showed the precipitates inside the dimples. The EDS analysis result indicated the carbide particles inside the dimple. The obtained fractograph showed the ductile mode of failure with slight shearing at the edges of the ruptured specimens.

Conflict of interest

The authors declare that they have no known competing financial interests or personal relationships that could have appeared to influence the work reported in this paper.

References

1. X.L. Bai, Q. Zhang, G.H. Chen, J.Q. Wang, J.J. Liu, and X.H. Yu et al., High Temperature Tensile Test and Creep Rupture Strength Prediction of T92/Super304H Dissimilar Steel Weld Joints, *Mater. High Temp.*, 2014, **31**, p 69–76. https://doi.org/10.1179/0960340913Z.0000000009

2. K. Nicol, *Status of Advanced Ultra-Supercritical Pulverised Coal Technology*, IEA Clean Coal Centre, Gloucester, 2013

3. A.K. Bhaduri, S. Venkadesan, P. Rodriguez, and P.G. Mukunda, Transition Metal Joints for Steam Generators-An Overview, *Int. J. Press. Vessel. Pip.*, 1994, **58**, p 251–265. https://doi.org/10.1016/0308-0161(94)90061-2

4. W. Zhang, T. Zhang, X. Wang, H. Chen, and J. Gong, Remaining Creep Properties and Fracture Behaviour of P92 Steel Welded Joint under Prior Low Cycle Fatigue Loading, *J. Mater. Res. Technol.*, 2020, **9**, p 7887–7899. https://doi.org/10.1016/j.jmrt.2020.05.078

5. M.Ş Adin and M. Okumuş, Investigation of Microstructural and Mechanical Properties of Dissimilar Metal Weld Between AISI 420 and AISI 1018 STEELS, *Arab. J. Sci. Eng.*, 2022, **47**, p 8341–8350. https://doi.org/10.1007/s13369-021-06243-w

6. M.Ş Adin, A Parametric Study on the Mechanical Properties of MIG and TIG Welded Dissimilar Steel Joints, *J. Adhes. Sci. Technol*, 2023 https://doi.org/10.1080/01694243.2023.2221391

7. G. Chen, Q. Zhang, J. Liu, J. Wang, X. Yu, and J. Hua et al., Microstructures and Mechanical Properties of T92/Super304H Dissimilar Steel Weld Joints After High-Temperature Ageing, *Mater. Des.*, 2013, **44**, p 469–475. https://doi.org/10.1016/j.matdes.2012.08.022

8. M. Amra, S.R. Alavi Zaree, and R. Dehmolaei, Dissimilar Welding Between 1.4742 Ferritic and 310S Austenitic Stainless Steels: Assessment of Oxidation Behaviour, *Met. Mater. Int.*, 2021, **27**, p 931–45. https://doi.org/10.1007/s12540-019-00485-y

9. Y. Zhang, H. Jing, L. Xu, Y. Han, L. Zhao, and B. Xiao, Microstructure and Mechanical Performance of Welded Joint Between a Novel Heat-Resistant Steel and Inconel 617 Weld Metal, *Mater. Charact.*, 2018, **139**, p 279–292. https://doi.org/10.1016/j.matchar.2018.03.012

10. J. Parker, In-service Behaviour of Creep Strength Enhanced Ferritic Steels Grade 91 and Grade 92–Part 2 Weld Issues, *Int. J. Press. Vessel. Pip.*, 2014, **114**, p 76–87.

11. J.H. Lee, J.H. Hwang, Y.S. Park, T.M. Kim, D.H. Bae, and W.B. Seo et al., Assessing Mechanical Properties of the Dissimilar Metal Welding Between P92 Steels and alloy 617 at High Temperature, *J. Mech. Sci. Technol.*, 2016, **30**, p 4453–4457. https://doi.org/10.1007/s12206-016-0911-1

12. E.I. Samuel, B.K. Choud, D.P.R. Palaparti, and M.D. Mathew, Creep Deformation and Rupture Behaviour of P92 Steel at 92 23 K, *Procedia Eng.*, 2013, **55**, p 64–69. https://doi.org/10.1016/j.proeng.2013.03.220

13. J. Cao, Y. Gong, and Z. Yang, Microstructural Analysis on Creep Properties of Dissimilar Materials Joints Between T92 Martensitic and HR3C Austenitic Steels, *Mater. Sci. Eng. A*, 2011, **528**, p 6103–6111. https://doi.org/10.1016/j.msea.2011.04.057

14. L. Falat, M. Svoboda, A. Výrostková, I. Petryshynets, and M. Sopko, Microstructure and Creep Characteristics of Dissimilar T91/TP316H Martensitic/Austenitic Welded Joint with Ni-based Weld Metal, *Mater. Charact.*, 2012, **72**, p 15–23. https://doi.org/10.1016/j.matchar.2012.06.014

15. T. Matsunaga, H. Hongo, and M. Tabuchi, Interfacial Failure in Dissimilar Weld Joint of High Boron 9% Chromium Steel and Nickel-Based Alloy under High-Temperature Creep Condition, *Mater. Sci. Eng. A*, 2017, **695**, p 302–308. https://doi.org/10.1016/j.msea.2017.04.012

16. Q. Wang, R. Xin, Z. Wang, Z. Han, X. Jiao, and J. Kang, Microstructure and its Effect on High Temperature Tensile Properties of T92/HR3C Dissimilar Weld Joints, *J. Manuf. Process.*, 2022, **82**, p 792–799. https://doi.org/10.1016/j.jmapro.2022.08.046

17. G. Chen, Y. Song, J. Wang, J. Liu, X. Yu, and J. Hua et al., High-Temperature Short-Term Tensile Test and Creep Rupture Strength Prediction of the T92/TP347H Dissimilar Steel Weld Joints, *Eng. Fail. Anal.*, 2012, **26**, p 220–229. https://doi.org/10.1016/j.engfailanal.2012.05.024

18. M.Y. Kim, S.C. Kwak, I.S. Choi, Y.K. Lee, J.Y. Suh, and E. Fleury et al., High-Temperature Tensile and Creep Deformation of Cross-Weld Specimens of Weld Joint Between T92 Martensitic and Super304H Austenitic Steels, *Mater. Charact.*, 2014, **97**, p 161–168. https://doi.org/10.1016/j.matchar.2014.09.011

19. K. Miao, J. Liu, Y. Yin, T. Wang, G. Sun, and C. Liu et al., Microstructure and Failure Analysis of TP347H/T91 Dissimilar Steel Welded Piping, *J. Fail. Anal. Prev.*, 2022, **22**, p 578–586. https://doi.org/10.1007/s11668-022-01349-1

20. F. Kabakcı, M. Acarer, M. Baydoğan, A. Selçuk Keskinkılıç, F.K. Acar, and H. Çimenoğlu, Effect of Co Addition on the Creep Rupture Properties of 9Cr-1.8W-xCo Weld Metals, *Metall. Mater. Trans. A Phys. Metall. Mater. Sci.*, 2021, **52**, p 129–142. https://doi.org/10.1007/s11661-020-06059-7

21. T. Sakthivel, G. Sasikala, M.K. Dash and R.P. Syamala, Creep Deformation and Rupture Behavior of P92 Steel Weld Joint Fabricated by NG-TIG Welding Process, *J. Mater. Eng. Perform.*, 2019, **28**, p 4364–4378. https://doi.org/10.1007/s11665-019-04157-1

22. E. Nandha Kumar, G.D. Janaki Ram, K. Devakumaran, and R.S. Kottada, Effect of Long-Term Exposure at 650 °C on Microstructural and Creep Characteristics of T92/Super304H dissimilar Welds, *Weld World*, 2020, **64**, p 467–81. https://doi.org/10.1007/s40194-019-00845-7

23. W. Xue, P. Qian-gang, R. Yao-yao, S. Wei, Z. Hui-qiang, and L. Hong, Microstructure and Type IV Cracking Behavior of HAZ in P92 Steel Weldment, *Mater. Sci. Eng. A*, 2012, **552**, p 493–501. https://doi.org/10.1016/j.msea.2012.05.076

24. Y. Huang, Y. Zhan, X. Luo, J. Xiong, J. Yang, and G. Mao et al., Creep Deformation and Rupture Behavior of 10Cr-3Co-2W Heat-Resistant Steel Weldments in Ultra Supercritical Power Units, *Eng. Fail. Anal.*, 2022, **133**, p 105984. https://doi.org/10.1016/j.engfailanal.2021.105984

25. X. Wang, X. Wang, Y.L. Zhang, C. Wang, Y. Li, and Q.S. Huang, Microstructure and Creep Fracture Behavior in HR3C/T92 Dissimilar Steel Welds, *Mater. Sci. Eng. A*, 2021, **799**, p 140128. https://doi.org/10.1016/j.msea.2020.140128

26. W. Liu, X. Liu, F. Lu, X. Tang, H. Cui, and Y. Gao, Creep Behavior and Microstructure Evaluation of Welded Joint in Dissimilar Modified 9Cr-1Mo Steels, *Mater. Sci. Eng. A*, 2015, **644**, p 337–346. https://doi.org/10.1016/j.msea.2015.07.068

27. G. Dak and C. Pandey, Experimental Investigation on Microstructure, Mechanical Properties, and Residual Stresses of Dissimilar Welded Joint of Martensitic P92 and AISI 304L Austenitic Stainless Steel, *Int. J. Press. Vessel. Pip.*, 2021, **194**, p 104536. https://doi.org/10.1016/j.ijpvp.2021.104536

28. G. Dak, N. Khanna, and C. Pandey, Study on Narrow Gap Welding of Martensitic Grade P92 and Austenitic Grade AISI 304L SS Steel for Ultra-Supercritical Power Plant Application, *Arch. Civ. Mech. Eng.*, 2023, **23**, p 14. https://doi.org/10.1007/s43452-022-00540-3

29. M.S. Rahman, G. Priyadarshan, K.S. Raja, C. Nesbitt, and M. Misra, Characterization of High Temperature Deformation Behavior of Inconel 617, *Mech. Mater.*, 2009, **41**, p 261–270. https://doi.org/10.1016/j.mechmat.2008.10.003

30. G. Sainath, B.K. Choudhary, J. Christopher, E. Isaac Samuel, and M.D. Mathew, Effects of Temperature and Strain Rate on Tensile Stress-Strain and Workhardening Behaviour of P92 Ferritic Steel, *Mater. Sci. Technol. (United Kingdom)*, 2014, **30**, p 911–920. https://doi.org/10.1179/1743284713Y.0000000349

31. B.R. Antoun, C. Alleman, and K. De La Trinidad, Experimental Investigation of Dynamic Strain Aging in 304l Stainless Steel, *Conf. Proc. Soc. Exp. Mech. Ser.*, 2019 https://doi.org/10.1007/978-3-319-95053-2_10

32. A. Zergani, H. Mirzadeh, and R. Mahmudi, Evolutions of Mechanical Properties of AISI 304L Stainless Steel under Shear Loading, *Mater. Sci. Eng. A*, 2020, **791**, p 139667. https://doi.org/10.1016/j.msea.2020.139667

33. A.K. Gupta, H.N. Krishnamurthy, Y. Singh, K.M. Prasad, and S.K. Singh, Development of Constitutive Models for Dynamic Strain Aging Regime in Austenitic Stainless Steel 304, *Mater. Des.*, 2013, **45**, p 616–627. https://doi.org/10.1016/j.matdes.2012.09.041

34. Y.M. Song, G.H. Chen, J.Q. Wang, J.J. Liu, X.H. Yu, and J. Hua et al., Short-Term High-Temperature Tensile Tests and Prediction of Long-Term Strength of Welded Joints Of Dissimilar Steels T92/HR3C, *Met. Sci. Heat Treat.*, 2014, **55**, p 614–621. https://doi.org/10.1007/s11041-014-9678-0

35. W. Xue, Q. Pan, Y. Ren, W. Shang, H. Zeng, and H. Liu, Microstructure and Type IV Cracking Behavior of HAZ in P92 Steel Weldment, *Mater. Sci. Eng. A*, 2012, **552**, p 493–501. https://doi.org/10.1016/j.msea.2012.05.076

36. D. Meng, F. Lu, H. Cui, Y. Ding, X. Tang, and X. Huo, Investigation on Creep Behavior of Welded Joint of Advanced 9%Cr Steels, *J. Mater. Res.*, 2014, **30**, p 197–205. https://doi.org/10.1557/jmr.2014.366

37. M. Godec and D.A.S. Balantič, Coarsening Behaviour of $M_{23}C_6$ Carbides in Creep-Resistant Steel Exposed to High Temperatures, *Sci. Rep.*, 2016, **6**, p 1–7. https://doi.org/10.1038/srep29734

38. R.K. Desu, H. Nitin Krishnamurthy, A. Balu, A.K. Gupta, and S.K. Singh, Mechanical Properties of Austenitic Stainless Steel 304L and 316L at Elevated Temperatures, *J. Mater. Res. Technol.*, 2016, **5**, p 13–20. https://doi.org/10.1016/j.jmrt.2015.04.001

39. M. Kim, S. Kwak, I. Choi, Y. Lee, J. Suh, and E. Fleury et al., Materials Characterization High-Temperature Tensile and Creep Deformation of Cross-Weld Specimens of Weld Joint Between T92 Martensitic and Super304H Austenitic Steels, *Mater. Charact.*, 2014, **97**, p 161–168. https://doi.org/10.1016/j.matchar.2014.09.011

40. ASTM International–E139, Standard Test Method for Conducting Creep, Creep-Rupture, and Stress-Rupture Tests of Metallic Materials, *Annu. B ASTM Stand.*, 2018, **11**, p 1–14. https://doi.org/10.1520/E0139-11R18.responsibility

41. G. Wu, K. Ding, T. Wei, S. Qiao, X. Liu, and Y. Gao, Rupture Behavior and Fracture Mode for Inconel 625-9% Cr Steel Dissimilar Welded Joints at High Temperature, *Eng. Fail. Anal.*, 2021, **125**, p 105412. https://doi.org/10.1016/j.engfailanal.2021.105412

42. J. Swaminathan, K. Guguloth, M. Gunjan, P. Roy, and R. Ghosh, Failure Analysis and Remaining Life Assessment of Service Exposed Primary Reformer Heater Tubes, *Eng. Fail. Anal.*, 2008, **15**, p 311–331. https://doi.org/10.1016/j.engfailanal.2007.02.004

43. A.H.V. Pavan, K.S.N. Vikrant, R. Ravibharath, and K. Singh, Development and Evaluation of SUS 304H-IN 617 Welds for Advanced Ultra Supercritical Boiler Applications, *Mater. Sci. Eng. A*, 2015, **642**, p 32–41. https://doi.org/10.1016/j.msea.2015.06.065

44. K.Y. Shin, J.W. Lee, J.M. Han, K.W. Lee, B.O. Kong, and H.U. Hong, Transition of Creep Damage Region in Dissimilar Welds Between Inconel 740H Ni-based Superalloy and P92 Ferritic/Martensitic Steel, *Mater. Charact.*, 2018, **139**, p 144–152. https://doi.org/10.1016/j.matchar.2018.02.039

45. Y.I. Gong, J. Cao, L. Ji, C. Yang, C. Yao, and Z. Yang et al., Assessment of Creep Rupture Properties for Dissimilar Steels Welded Joints Between T92 and HR3C, *Fatigue Fract. Eng. Mater. Struct.*, 2010, **34**, p 83–96. https://doi.org/10.1111/j.1460-2695.2010.01496.x

46. Y. Wang, C. Shao, M. Fan, N. Ma, and F. Lu, Effect of Solidified Grain Boundary on Interfacial Creep Failure Behavior for Steel/Nickel Dissimilar Metal Welded Joint, *Mater. Sci. Eng. A*, 2021, **803**, p 140482. https://doi.org/10.1016/j.msea.2020.140482

47. X. Wang, X. Wang, H. Li, H. Wu, Y. Ren, and H. Liu et al., Laves Phase Precipitation Behavior in the Simulated Fine-Grained Heat-Affected Zone of Creep Strength Enhanced Ferritic Steel P92 and its Role in Creep Void Nucleation and Growth, *Weld World*, 2017, **61**, p 231–239. https://doi.org/10.1007/s40194-017-0424-2

48. G. Dak and C. Pandey, A Critical Review on Dissimilar Welds Joint Between Martensitic and Austenitic Steel for Power Plant Application, *J. Manuf. Process.*, 2020, **58**, p 377–406. https://doi.org/10.1016/j.jmapro.2020.08.019

49. K. Bong Yoon, V. Lok, T. Le Giang, Yu.J. Min, Y. Wha Ma, and V. Phu Nguyen et al., Changes in Creep Property and Precipitates Due to Aging of T91 Steel After Long-Term Service, *J. Mech. Sci. Technol.*, 2020, **34**, p 2020. https://doi.org/10.1007/s12206-020-07

50. C.C. Silva, M.H.C. De, M.F. Motta, J.P. Farias, C.R.M. Afonso, and A.J. Ramirez, New Insight on the Solidification Path of an Alloy 625 Weld Overlay, *J. Mater. Res. Technol.*, 2013, **2**, p 228–237. https://doi.org/10.1016/j.jmrt.2013.02.008

51. Y. Zhang, K. Li, Z. Cai, and J. Pan, Creep Rupture Properties of Dissimilar Metal Weld Between Inconel 617B and Modified 9%Cr Martensitic Steel, *Mater. Sci. Eng. A*, 2019, **764**, p 138185. https://doi.org/10.1016/j.msea.2019.138185